Performance Optimization of a Cation-Disordered Rock-Salt Positive Electrode Material for Next-Generation Lithium-ion Batteries

by

Storm William D Gourley

A thesis
presented to the University of Waterloo
in fulfillment of the
thesis requirement for the degree of
Master of Applied Science
in
Chemical Engineering

Waterloo, Ontario, Canada, 2020

Author's Declaration

I hereby declare that I am the sole author of this thesis. This is a true copy of the thesis, including any required final revisions, as accepted by my examiners.

I understand that my thesis may be made electronically available to the public.

Abstract

The growing threat of climate change has sparked a shift in societal norms surrounding the reliance on fossil fuels for our energy and transportation sectors. Driven by this shift, the global demand for sustainable energy sources and advanced energy storage technologies has seen a considerable increase over the last decade. In particular, electrification of the automotive industry coupled with the continued growth of the consumer electronics market and the need for stabilization of intermittent energy sources at the grid level has caused an unparalleled increase in utilization of lithium-ion batteries.

Electric vehicle sales in 2016 represented only 0.2% of the market share but is anticipated to reach over 86% by 2060. Further market penetration of electric vehicles is currently inhibited by the battery pack performance and cost, due to the limitations of modern batteries and the use of expensive raw materials. The potential growth of this market has galvanized research efforts to improve the cost-to-range ratio of lithium-ion batteries for use in next-generation electric vehicles.

The focus of these efforts has primarily been in the development of new electrode materials and the improvement of those already commercialized. Disordered rocksalts are an emerging class of positive electrode material for lithium ion batteries that offers high energy density (~1000Wh.kg^{-1}) capable of meeting range targets set for future electric vehicles. Although this material has promising energy metrics, DRX cathodes suffer from low electrochemical stability and poor rate performance that inhibit their deployment in modern applications.

This thesis focuses on improving the cycling stability of a DRX cathode, $Li_{1.25}Mn_{0.5}Nb_{0.25}O_2$, through the modification of particle morphology. This work presents an optimized synthesis pathway for the formation of single crystal particles with increased structural stability. The use of surface coatings is also examined as a strategy to improve the rate performance and surface level stability of the DRX material. Physical and electrochemical results for the series of prepared cathodes are detailed and new insight into the potential of these strategies to push DRX materials towards commercialization is discussed.

Acknowledgements

I would like to thank my supervisor Professor Zhongwei Chen for giving me the opportunity to work on such an interesting project and providing lab space and equipment for my experiments. I would also like to acknowledge Hao Liu for his guidance and support throughout the course of this project and Tyler Or for his help problem solving and brainstorming. Moreover, I would like to acknowledge the help many of my colleagues in the Applied Nanomaterials & Clean Energy Laboratory over the last 2 years.

Special thanks to my parents for trusting in me to accomplish the goals I set for myself and for providing me with ample support at all stages of my education. I also want to express my gratitude to Qian Shi for always encouraging me, being my motivation to keep going and for being by my side every step of the way. Finally, to my friends Timothy Wong and Aravind Ramaraju for our countless late-night discussions and their support as we went through this process together.

Table of Contents

List of Figures

List of Tables

List of Abbreviations

Ah	Ampere hours
ALD	Atomic Layer Deposition
ARC	Accelerating Rate Calorimetry
BMF	Blown microfiber
BSE	Back Scattered Electrons
C	Charge/discharge rate (1C = 1 hour charge/discharge)
CAGR	Compound Annual Growth Rate
CC	Constant Current
CV	Constant Voltage
CE	Coulombic Efficiency
DMF	N, N-dimethylformamide
DOD	Depth of Discharge
DRX	Disordered Rocksalts
E1	Electrode preparation method 1
E2	Electrode preparation method 2
E3	Electrode preparation method 3
EC	Ethylene Carbonate
EDX	Energy dispersive x-ray spectroscopy
EIS	Electrochemical impedance spectroscopy
EMC	Ethyl methyl carbonate
eV	Electron volt
EV	Electric Vehicle
GWh	Gigawatt hours
HEV	Hybrid Electric Vehicle
HF	Hydrofluoric acid
kPa	kilopascal
LBCO	$2Li_2O$-B_2O_3 coating
LCO	$LiCoO_2$ cathode
LFP	$LiFePO_4$ cathode

LIB	Lithium-ion battery
LMNO	$Li_{1.25}Mn_{0.5}Nb_{0.25}O_2$ cathode
mA	Milliamp
$mAh.g^{-1}$	Milliamp hours per gram
NCA	$Li[Ni_{1-x-y}Co_xAl_y]O_2$ ($x + y < 0.2$) cathode
NMC	$Li[Ni_xMn_yCo_z]O_2$ ($x + y + z = 1$) cathode
NMP	1-methyl-2-pyrrolidone
OCV	Open Circuit Voltage
PAN	polyacrylonitrile
psi	Pounds per square inch
PTFE	polytetrafluoroethylene
PVDF	poly(vinylidene fluoride)
PVP	polyvinylpyrrolidone
RPT	Reference Performance Test
SEI	Solid Electrolyte Interface
SEM	Scanning Electron Microscopy
SWCNT	Single Walled Carbon Nanotubes
TEM	Transmission Electron Microscopy
TGA	Thermogravimetric Analysis
TM	Transition Metal
TMA	trimethylaluminum
VC	Vinylene carbonate
$Wh.kg^{-1}$	Watt hours per kilogram
XRD	Powder X-ray Diffraction

List of Symbols

Å	Angstrom (unit of length)
^{o}C	Degrees Celsius (unit of temperature)
µm	Micrometer (length)
µl	Microliter (volume)
Θ	Diffraction Angle
λ	Wavelength
K	Constant in Eqn 2.3
re Z	Real component – electrochemical impedance as a function of frequency
im Z	Imaginary component – electrochemical impedance as a function of frequency

1. Introduction

1.1 Motivation

Over the past decade, the threat of climate change has become an increasingly relevant global issue, with media attention causing pressure on governments worldwide to adjust their environmental policies. In an effort to reduce the harmful effects of climate change on our planet, the need to decrease our reliance on conventional fossil fuels has made way for the promotion of renewable, ecofriendly energy sources (*e.g.* wind, solar, geothermal). However, the grid level exploitation of these energy sources has been limited due to the intermittency in energy production causing a disparity between supply and demand. The use of rechargeable batteries, lithium-ion batteries (LIBs) in particular, as a means to stabilize the deliverable supply of these sources is seen as one possible solution; however, the energy density of conventional LIBs is not high enough to make this a practical option. This imposes the need to develop high-energy density, inexpensive battery materials for grid level energy storage.

A more prominent use of LIBs in the past several years is due to the electrification of the automotive industry following a shift away from the use of internal combustion engine vehicles that rely on fossil fuels in favor of hybrid and fully electric vehicles (HEV/EVs). Globally, EV sales have increased from <10,000 automobiles in 2010 to 774,000 in 2016 with cumulative sales surpassing 2 million, giving EVs a market share of 0.2%.[1] Continued growth of the EV market share is anticipated in order to conform to the Beyond 2 Degrees Scenario set by the International Energy Agency as a pathway to limiting global temperature increase to 1.75^{o}C.[2] This scenario calls for 1.8 billion cumulative EV sales by 2060 corresponding to an 86% market share and near complete electrification of the automotive industry. Following this growth, battery utilization has

increased by 30% annually from 2010 to reach a volume of 180 GWh in 2018 and is anticipated to continue growing at 25% annually in accordance with the aforementioned EV market share to an estimated 2600 GWh by 2030 as shown in **Figure 1**.[3]

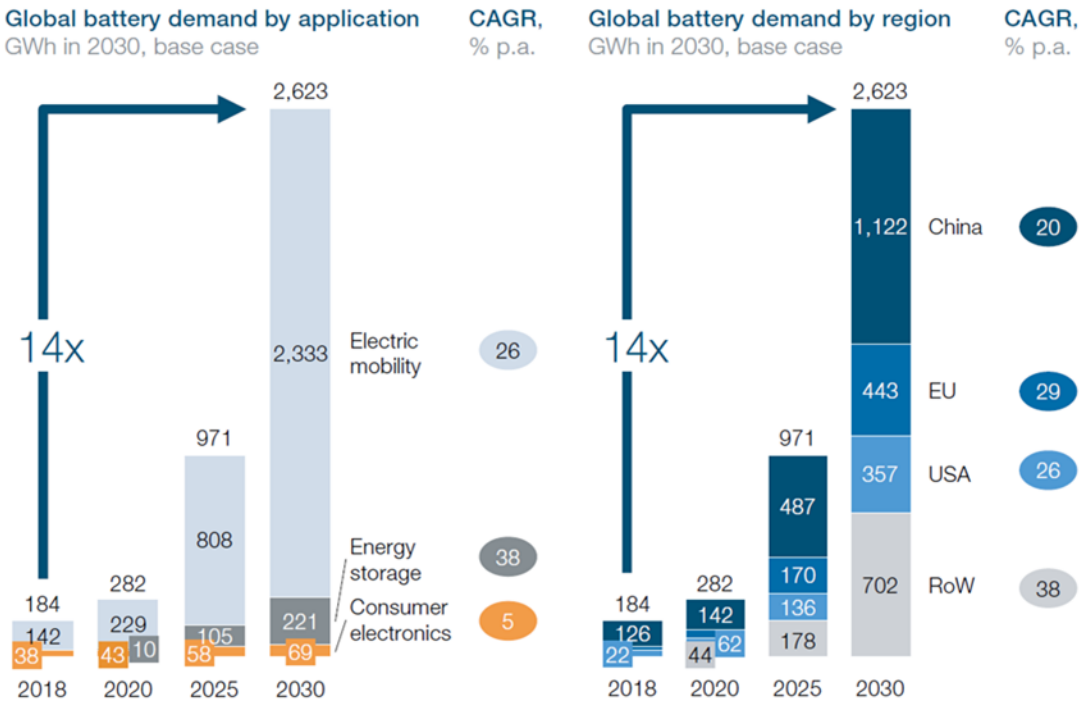

Figure 1 - Comparison of actual and anticipated global battery demand per year based on application and region.[3]

The combination of high energy and power density have made LIBs the most promising energy storage technology for EVs; however, further development of commercialized LIBs is required in order to meet the performance targets set for the next generation of EVs. Future adoption of EVs necessitates the improvement of cost-to-range ratio, safety rating (EUCAR scale), and charging time of modern EVs, with a particular emphasis placed on increasing the electric driving range above 300 miles.[1,4,5] Subsequently, this potential industry growth has galvanized research effort on conventional LIB cathode materials particularly those that have already been adopted by EV

manufacturers (*e.g.* Tesla Inc., BMW, Nissan, *etc.*).[6–9] Despite the performance advancements being made, the cost of LIBs remains a major barrier to further EV adoption. The reliance on expensive raw materials in conventional LIBs such as cobalt ($13.09 USD/lb) is a primary contributor to this issue and the need for cheaper materials is apparent.[10] Additionally, the utilization of cobalt is associated with socioeconomic concerns owing in part to the instability of the monopolistic nature of the supply chain and the lack of regulatory standards in primary mining and manufacturing locations.[3] In 2017, the European Union listed cobalt as a critical raw material with a potential supply risk due to the low substitution and recycling rates as well as an increasing production capacity for cobalt containing LIBs.[11,12] In response to these concerns increased efforts have been made to develop cobalt-free LIB technologies that not only reduce the cost of the battery but improve upon its performance to meet the targets set for next-generation EVs.

This thesis focuses on an emerging class of high-energy density, cobalt-free cathode for LIBs by providing insight to cation-disordered rock-salt (DRX) materials. The objective of this project is to optimize the electrochemical performance of the battery by modifying the synthesis methodology and applying various surface treatments/coatings to the cathode material. The focus of this thesis will be on the $Li_{1.25}Mn_{0.5}Nb_{0.25}O_2$ cathode composition, which is referred to as LMNO throughout the rest of the report. The effects of milling technique, sintering temperature, time, and lithium content during synthesis of the LMNO material will be investigated as well as the impact that the direct substitution of Mn for Ni has on the capacity and stability of the battery. A systematic analysis of surface treatments and coatings including solvent casting of polyacrylonitrile (PAN), atomic layer deposition (ALD) of alumina (Al_2O_3), and solid-state synthesis of an Li_2O-B_2O_3 (LBCO) composite on the cycling performance and rate capability of

the battery will also be conducted. Performance of the materials is evaluated using a range of both physical and electrochemical characterization techniques with the results detailed herein.

1.2 Lithium-ion Batteries

Batteries are a type of electrochemical power source that facilitate the conversion of chemical potential to electrical energy either irreversibly (primary battery) or reversibly (secondary battery).[13] Primary batteries are designed to be discarded after a single use as they completely deplete the initial material in order to produce electricity. In contrast, the reactions that occur within secondary batteries are reversible, enabled by the application of an external power source to pass electricity through the battery, otherwise known as charging. Both types of batteries have a unique set of advantages and disadvantages; however, this thesis will focus only on secondary batteries as LIBs fall within that classification.

1.2.1 Operating Principles and Components

LIBs are composed of a positive electrode (cathode) and negative electrode (anode) placed in series with one another acting as an insertion host network for Li^+ ions. The electrodes are separated by an ionically conductive material known as an electrolyte and a polymeric separator layer. During charging the battery stores energy from an externally applied source through an oxidation reaction, or loss of electrons, at the positive electrode to enable the diffusion of Li^+ ions through the electrolyte towards the negative electrode which then undergoes a reduction reaction, or gain of electrons, storing the Li^+ ions within its structure. When discharging, the battery produces a useable electric current driven by the reverse process with a reduction reaction at the positive electrode and oxidation reaction at the negative electrode.[14–16] An example of this process

using Li_xCoO_2 as the cathode is shown in Eqn (1.1) below, where the crystal lattice is oxidized when charging and reduced when discharging. The corresponding reaction for a carbon-based anode is shown in Eqn (1.2).

$$LiCoO_2 \leftrightarrow Li_{1-x}CoO_2 + xLi^+ + xe^- \quad (1.1)$$

$$xLi^+ + xe^- + 6C \leftrightarrow Li_xC_6 \quad (1.2)$$

Conventional cathode active materials responsible for intercalation of Li^+ are mixed with a polymeric binder (*e.g.* polytetrafluoroethylene, polyvinylidene fluoride) to increase structural stability, and a carbon based additive to improve the electrical conductivity of the electrode. Furthermore, in order to properly apply or utilize electric current within the battery, both the anode and cathode are coated onto an electrically conductive current collector (*e.g.* aluminum, copper).

Electrolytes are typically liquid, being composed of lithium salts (*e.g.* $LiClO_4$, $LiAsF_6$, $LiPF_6$) dissolved in a single or mixture of non-aqueous solvents (*e.g.* ethylene carbonate, diethyl carbonate, ethyl methyl carbonate). Electrolytes have a high ionic conductivity and facilitate the diffusion of Li^+ ions between electrodes during charge and discharge.[17] Although solid-state electrolytes are attracting considerable interest for use in batteries for thin, flexible devices, the technology is not widely considered for use in modern EVs.[18,19] When a liquid electrolyte is used a physical separator is needed to prevent direct contact of the cathode and anode, which would short-circuit the battery, while still allowing for the transport of Li^+ ions. **Figure 2** illustrates the components and operation of a conventional LIB.

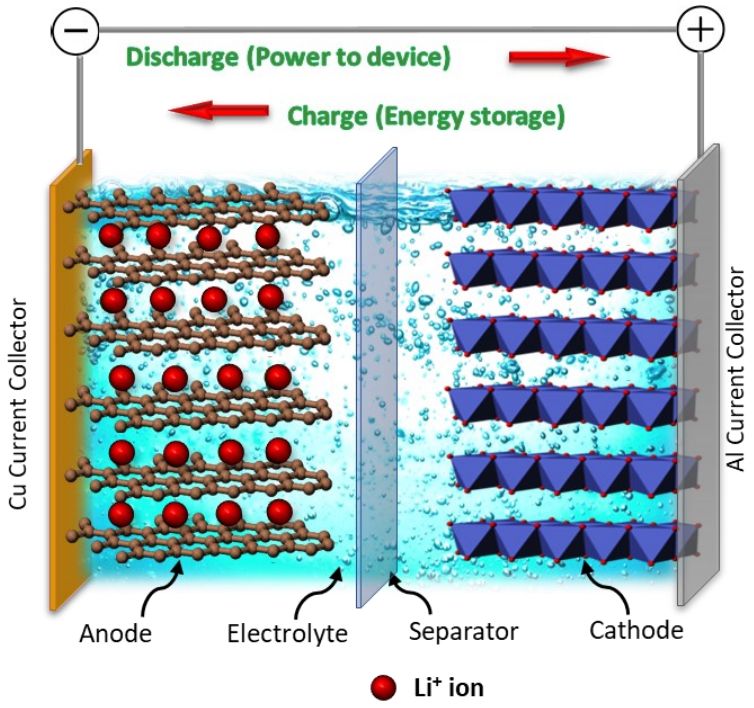

Figure 2 - Schematic of lithium-ion battery operation

1.2.2 Performance Characterization

Battery performance is characterized through several quantifiable metrics. In terms of electrochemical performance, the capacity of the battery is the total amount of charge stored in the material and is measured as the amount of time that the battery can deliver a current equal to the discharge rate at the nominal voltage of the battery with units of ampere-hours (Ah). In research, the capacity of the battery is commonly measured in terms of the active material mass ($mAh.g^{-1}$). The energy density, measured in watt-hours per kilogram ($Wh.kg^{-1}$), is a quantification for the deliverable electrical energy and is calculated by taking the product of the capacity and nominal voltage of the battery. The stability of the battery is measured as the number of cycles that it can be charged and discharged without considerable loss of capacity; in commercialized batteries the end-of-life is usually defined to occur when the discharge capacity drops below 70-80%. The rate

performance or rate capability of the battery is a measure of how quickly it can be charged or discharged. This metric is reported in terms of the deliverable capacity at a given current (mA) or C-rate, where 1C is the current required to fully charge or discharge the battery in 1 hour. In addition to the electrochemical performance, the safety of the battery is key especially for use in consumer electronics or EVs. The safety of the battery can be evaluated in many way (*e.g.* puncture tests, forced short-circuits, high voltage or elevated temperature cycling, etc.); however, the most common is to measure the maximum self-heating rate of the battery components ($^{o}C.min^{-1}$), as the temperature is increased over a given range. A lower rate at an elevated temperature corresponds to better battery safety, while a rate that increases exponentially at lower temperature is a sign of thermal runaway. These characteristics are all critical in determining the viability of the battery for commercialization in EVs and their improvement is necessary for further electrification of the automotive industry as a whole.

1.2.3 Lithium-ion Battery Cathodes

A common method of classification for LIBs is based on the atomic composition and lattice structure of their positive electrode material. Despite having different compositions, the ion diffusion pathways for conventional lithium insertion compounds are limited to layered, spinel, or olivine type lattice structure as illustrated in **Figure 3**. Several compositions that do not fall into one of these lattice types have recently emerged and will be discussed in section.

Layered structures often have the form $LiMO_2$ (M = Ni, Co) and separate lithium and transition metal oxides into a stack of alternating slabs. Layered cathodes are a part of the rhombohedral structural family (*R3m* space group) with oxygen ions forming a cubic closed packed (ccp)

arrangement and lithium and transition metal ions occupying octahedral sites of the alternating layers. The position of oxygen in parallel layers (stacking) is responsible for the local environment of the lithium and transition metal ions. For example, a common stacking arrangement is ABCABC which forms an O3-type oxide packing and forces the ions into octahedral sites. However, if the stacking sequence is ABAB then a T1-type oxide packing is formed denoting the presence of two tetrahedral sites instead.[20] The most prominent layered oxide cathodes in modern applications are $LiCoO_2$ (LCO), $Li[Ni_xMn_yCo_z]O_2$ ($x + y + z = 1$) (NMC), and $Li[Ni_{1-x-y}Co_xAl_y]O_2$ ($x + y < 0.2$) (NCA).[21] Layered cathodes allow for Li-ion diffusion in two dimensions through the interlayer space while spinel cathodes differ by enabling the diffusion of Li-ions in three dimensions through a 3D network. Spinel compounds are often Mn-based (*e.g.* $LiMn_2O_4$), crystallizing into the *Fd3m* space group with oxygen ions forming a ccp lattice arrangement. $LiFePO_4$ (LFP) is the most notable example of an olivine type cathode material due to its commercialization in electric buses and stationary energy storage systems. LFP is a part of the orthorhombic structural family (*Pnma* space group) with oxygen ions forming a hexagonal closed packed (hcp) framework that contains Li and Fe atoms in octahedral sites and P atoms in tetrahedral sites.[22] Unlike the layered and spinel type cathodes, lithium-ion diffusion in olivine structures occurs only in one dimension due to the formation of rod-like channels within the lattice network.

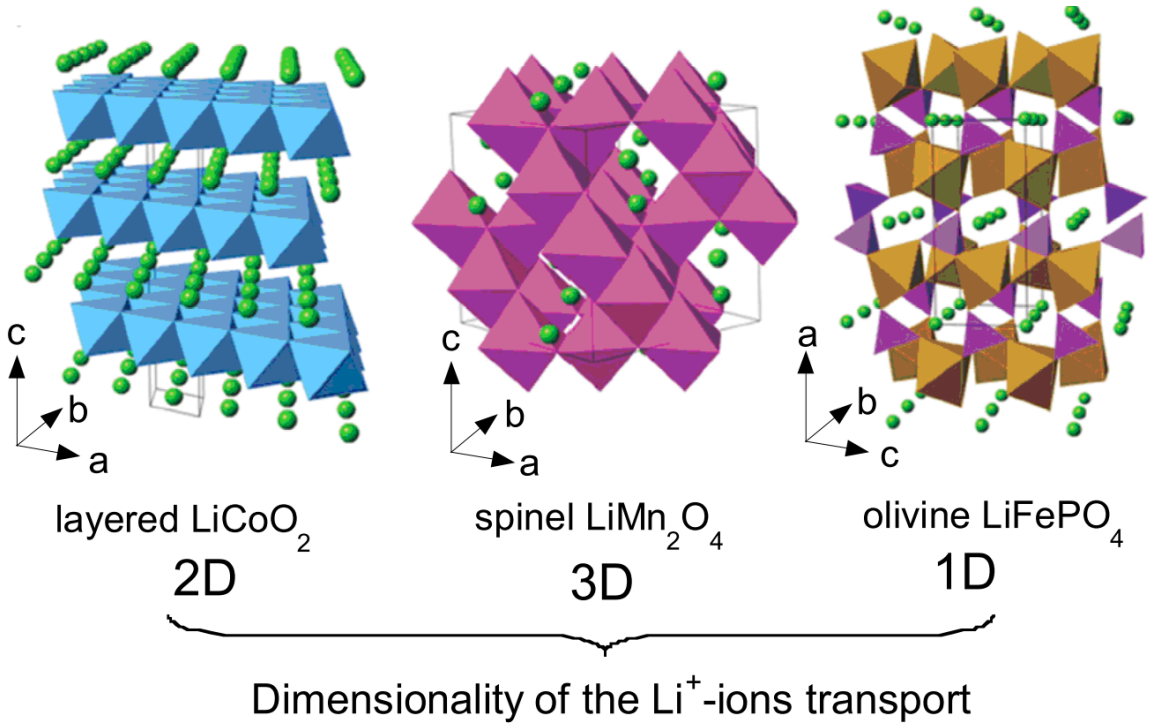

Figure 3 - Schematic of the dimensionality and structure for three types of lattice structure of LIB cathodes. Left: layered $LiCoO_2$; Mid: spinel $LiMn_2O_4$; Right: olivine $LiFePO_4$[23]

1.2.4 Battery Degradation

The initial performance of a battery is often associated with its highest possible performance. Throughout charge and discharge operation, the components of the battery will degrade in different ways detrimentally affect its performance; however, to remain within the scope of this thesis, only degradation mechanisms associated with the electrodes will be discussed. In general, degradation can be categorized as either capacity fade or impedance growth, although both lead to the inevitable loss of performance. Capacity fade is typically associated with the disintegration of the cathode material or the loss of lithium inventory, while impedance growth factors in the formation of passivated surface layers and contact deterioration.

Surface Reconstruction

Electrolytes used in LIBs are typically composed of a Li-based salt (*e.g.* $LiPF_6$) and an organic solvent. Reduction of this electrolyte at the surface of the electrode during the first charge causes the formation of a passivated film known as the solid electrolyte interphase (SEI). The formation of an SEI is a regular phenomenon when charging the battery; however, the stability of this phase is critical to the longevity of the battery as degradation of the SEI can cause dissolution of the cathode active material leading to a loss of capacity.[17] Furthermore, parasitic reactions during cycling lead to the immobilization of Li^+ within the SEI and an increased polarization causing a virtual potential, raising the charge voltage and decreasing the discharge voltage of the battery, that reduces its overall energy density.[24,25]

In layered structures the transition metal and lithium ions are located in specific sites within the lattice making up the distinct layers. However, this can be disrupted when transition metal ions such as Ni^{2+} are used in the composition as magnetic frustration within the lattice gives rise to instability of the structure and forces the intermixing of non-magnetic Li^+ to alleviate the frustration.[26] The similar radius of Li^+ (0.76Å) and Ni^{2+} (0.69 Å) allow an interchange of the ions within their lattice sites causing an irreversible loss of capacity due to loss of useable Li^+ inventory. As degree of delithiation is increased, the material reversibly transitions from a layered *R3m* to a spinel *Fd3m* structure; however, with increased mixing the surface of the particles can irreversibly transition from spinel *Fd3m* to a NiO-type rocksalt *Fm3m* structure.[27–29] As NiO is known to have low ionic and electrical conductivity, this transformed phase acts as a resistive layer that contributes to impedance rise within the system and a decreased deliverable capacity.[30]

Lattice Expansion and Contraction

Insertion and extraction of Li^+ ions from a layered oxide cathode structure causes expansion and contraction of the unit cell. The amount of volumetric change in the unit cell is dependent on the Li content in the cathode which changes during charge and discharge. At a higher degree of (de)lithiation (*i.e.* 100% DOD), which is required to achieve improved energy density in LIBs, the strain on the lattice is much greater. In particular, a phase change from the hexagonal 2 (H2) to hexagonal 3 (H3) phase that occurs around 4.2V vs. Li^+/Li is responsible for sharp contraction of the unit cell. This sharp anisotropic strain on the lattice and the poor reversibility of this phase transition can lead to the generation of microcrack defects at the particle surface.[30,31] As the battery is cycled, these cracks propagate into the bulk of the particle enabling electrolyte infiltration and increasing the surface area available for passivation through one of the surface reconstruction mechanisms discussed previously. Particle cracking causes an increased consumption of lithium that leads to an irreversibly reduced capacity and has been reported as a precursor mechanism to lattice collapse, and inevitably the complete degradation of the material (Figure 4). Additionally, intergranular cracking causes a loss of contact between the grains of secondary particles giving rise to an increased impedance in the battery.[32]

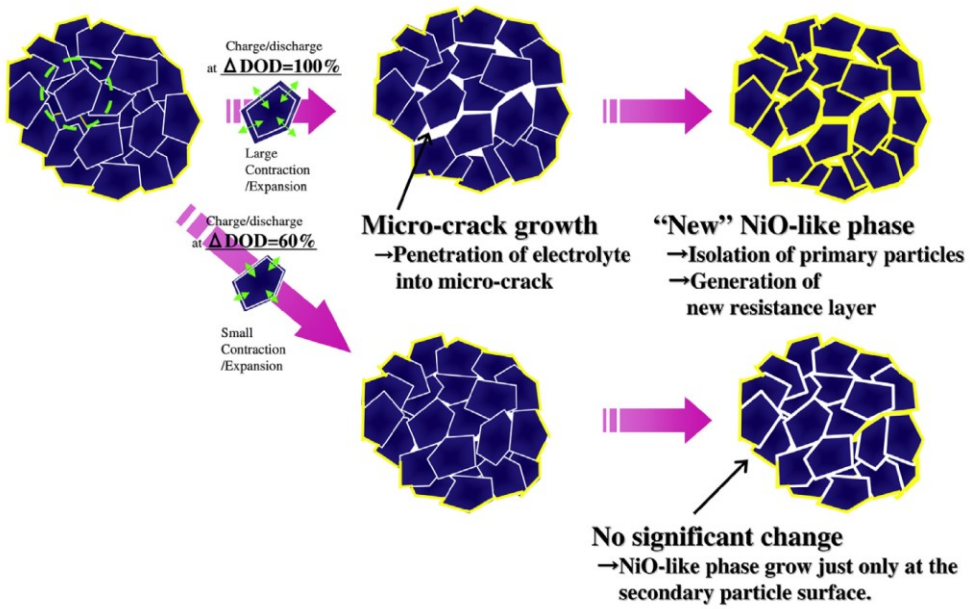

Figure 4 - Schematic of particle cracking in Ni-rich cathode materials during charge/discharge with depth of discharge (DOD) at 60% and 100%. [30]

Oxygen Loss

During the cycling operation of an intercalation cathode, lithium vacancies are regularly created and filled resulting in temporary point defects. Although the formation of these vacancies is desired in LIBs, the generation of unwanted vacancies within the lattice can also occur.[33] The tendency for unwanted vacancy formation increases as the battery is operated at an elevated voltage (>4.5V vs. Li^+/Li). As the delithiation continues and the voltage increases beyond 4.5V anionic oxidation ($O^{2-} \rightarrow O_2^{2-}$) occurs to charge compensate diffusion of excess Li^+, this allows for elevated capacity but also generates a reactive oxygen (O^-/O_2^{2-}) species. This species initiates the formation of a resistive interfacial layer on the particle surface through electrolyte decomposition and oxygen gas evolution, leaving an oxygen vacancy on the surface.[34,35] Further degradation is induced during cycling as these vacancy defects are injected into the particle bulk ultimately resulting in structural deterioration and lattice collapse, and rapid decrease in battery performance.[36]

1.2.5 Single and Polycrystalline Morphology

Conventional cathode materials for LIBs are made up of large secondary particles (~5-15µm diameter) that are agglomerates of small grains (~200-500nm) and are considered "polycrystalline". Polycrystalline materials have different size and orientation to each grain or crystallite determined by the local (short-range) atomic periodicity within the crystal. In contrast, "monocrystalline" or single crystal materials have infinite (long-range) atomic periodicity within the crystal leading to a large particle with the absence of grain boundaries. Figure 5 shows a schematic of the differences between a single crystal and polycrystalline particle.

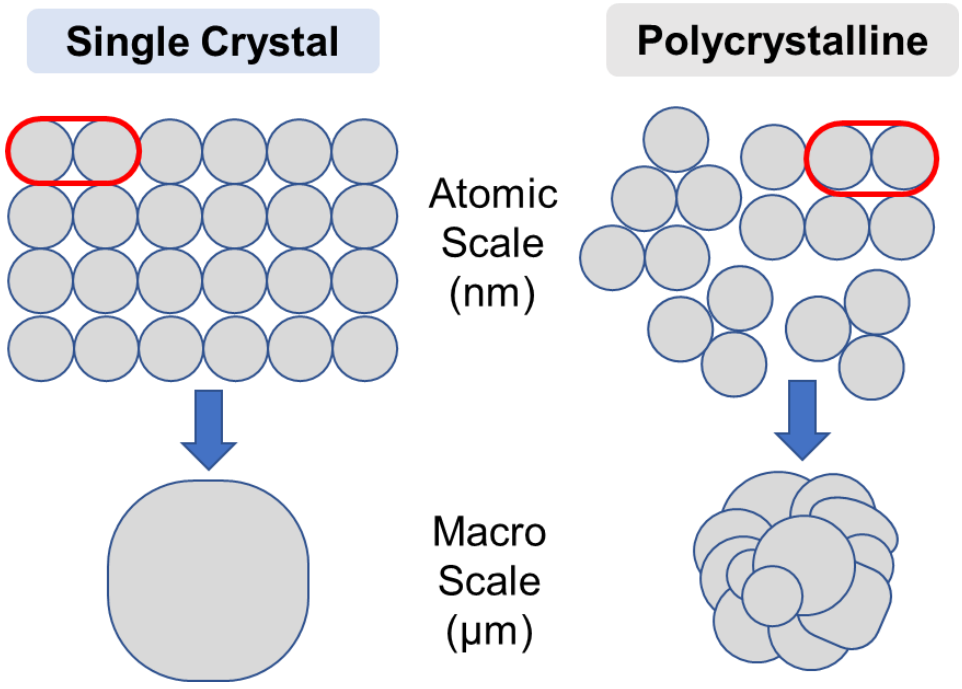

Figure 5 - Schematic diagram of atomic and microscopic differences between single crystal and polycrystalline particle.

The lack of a faceted appearance in the single crystal particle is associated with the growth of the particle with long-range atomic ordering which is in direct contrast to the polycrystalline particle

which clearly exhibits a well faceted surface. The development of single crystal cathode materials for LIBs has attracted considerable interest over the past several years and notable improvements to the structural stability of the batteries have been attributed to this adjusted morphology.[9,37,38]

1.3 Positive Electrode Materials for Lithium-ion Batteries

This section will highlight several well commercialized layered, spinel, and olivine cathode compositions that are used in modern consumer electronics and passenger or commercial EVs, detailing the specific advantages and disadvantages of each material in terms of performance or socioeconomic status.

1.3.1 $LiCoO_2$ (LCO)

$LiCoO_2$ (LCO) is a type of layered oxide positive electrode material first developed in 1980 by Goodenough *et al*. [39] Due to its performance in comparison to other batteries, LCO attracted a considerable amount of attention and was used by Sony in 1990 in the first commercial LIBs.[40] LCO continues to dominate the modern consumer electronics market, having the most success with portable devices, such as in the majority of smart phones.

The alternating Li and CoO_2 layers form two-dimensional diffusion channels allowing for high Li^+ ion diffusivity ($5x10^{-9}$ $cm.s^{-1}$) contributing to the rate capability of the material.[14] LCO typically operates over the voltage range of 3.0-4.2V vs. Li^+/Li with the cathode being fully lithiated, $LiCoO_2$, in the discharged state (3.0V) and half-lithiated, $Li_{1-x}CoO_2$ (x=0.4, 0.5) in the charged state (4.2V). Despite the high theoretical capacity of LCO at 270$mAh.g^{-1}$, the practical capacity is limited to 130-150$mAh.g^{-1}$ as delithiation of x>0.5 will cause irreversible structural change and

accelerated degradation of the electrode. Recent studies have developed modified LCO through ion-doping that improves the deliverable capacity to 190mAh.g^{-1}; however, further research is needed to enhance the performance of the material for higher energy density applications such as EVs.[41] The high cobalt content is another disadvantage of LCO as the raw material cost leads to a more expensive battery. When coupled with the poor cycle life and low thermal stability of the material it is clear that its current state is not ideal for EV applications. Battery recycling can partially offset the cost of the material as recycling 1 metric ton of LCO can produce up to $8900 in value, over 10 times the amount yielded from recycling $LiMn_2O_4$ batteries at $890.[42,43] However, further incentives are needed in order for current recycling plants to be profitable which is limiting the global adoption of battery recycling infrastructure.

1.3.2 $LiFePO_4$ (LFP)

$LiFePO_4$ (LFP) is an olivine type material that makes use of large phosphate (PO_4^{3-}) groups for charge compensation during delithiation of the material.[44] LFP was first developed by Goodenough's research group in 1997 as a low cost, environmentally friendly alternative cathode for LIBs.[45] LFP is a considerably cheaper positive electrode material than cobalt-containing alternatives, particularly LCO, owing to the use of naturally abundant elements.

The practical capacity of commercialized LFP batteries is typically ~120-160mAh.g^{-1} at a 100% depth of discharge (DOD), which is slightly lower than the theoretical capacity of 170mAh.g^{-1}. In contrast to the single-phase lithiation of LCO, LFP experiences a two-phase lithiation at 3.5V vs. Li^+/Li offering an extremely stable, flat charge/discharge profile. The cycling stability of LFP coupled with low-cost and increased thermal stability due to the covalent phosphate moieties make

it a promising candidate for application in EVs. However, poor ionic conductivity intrinsic to olivine materials and the low electronic conductivity of the composition are responsible for the rate capability issue of LFP that is a barrier for its further use in EVs. Several strategies for improving the conductivity have been investigated including carbon-coating surface of primary particles,[46] and reducing the average particle size.[47] Smaller particle size improved electrical percolation but decreased the tap density of the material giving the electrodes a low volumetric capacity. The carbon-coating strategy has been more promising, with studies reporting LFP electrodes capable of delivering a capacity well beyond the theoretical limit (208mAh.g^{-1}), enabled by the reversible reduction-oxidation reaction between Li^+ ions and the exfoliated graphene coated on the particle surface.[48]

LFP has generated interest in the public transportation sector and for stationary energy storage where cost, safety, and stability are more relevant factors than energy density.[49] Electric buses in particular utilize LFP batteries. Although not yet widely adopted in North America, they have seen successful deployment in China leading to idea that LFP will be an important material for the complete electrification of the automotive industry.[50]

1.3.3 $LiNi_xMn_yCo_zO_2$, $x + y + z = 1$ (NMC)

$LiNi_xMn_yCo_zO_2$ (NMC) is a family of layered transition metal oxide materials originally developed in 2001 by Ohzuku *et al.* after investigating lithium nickel manganese oxide materials with cobalt substitution as an alternative to the expensive $LiCoO_2$ cathode that dominated the LIB market.[51,52] NMC consists primarily of Ni^{2+}, Mn^{4+}, and Co^{3+} cations in varying proportions, the most popular of which are $LiNi_{1/3}Mn_{1/3}Co_{1/3}O_2$ (NMC111) and $LiNi_{0.5}Mn_{0.3}Co_{0.2}O_2$ (NMC532);

however, as higher energy densities and lower reliance on cobalt are necessary for next-generation LIBs Ni-rich compositions such as $LiNi_{0.6}Mn_{0.2}Co_{0.2}O_2$ (NMC622), and $LiNi_{0.8}Mn_{0.1}Co_{0.1}O_2$ (NMC811) are becoming more relevant.[21,53]

The fraction of Ni in the structure affects the deliverable capacity as charge compensation for Li^+ extraction and insertion are primarily due to Ni oxidation and reduction (redox) processes. The Mn^{4+} ions are electrochemically inactive in this composition serving to improve thermal and structural stability over that of $LiCoO_2$ cathodes. The presence of Co^{3+} contributes to the stability of the cathode structure through the suppression of cation mixing between Ni^{2+} and Li+ ions, as well as increases the electrical conductivity leading to a high rate capability. NMC111 has the greatest fraction of Mn^{4+} giving it the greatest thermal stability; however, its practical capacity is limited to 160 $mAh.g^{-1}$ when cycled over the voltage range of 2.7-4.3V vs. Li^+/Li. Increasing the Ni content allows for a greater degree of delithiation resulting in higher capacity over the same voltage range in materials such as NMC622 (180 $mAh.g^{-1}$) and NMC811 (200 $mAh.g^{-1}$).[54] This highlights an important trade-off between capacity and stability for NMC-type materials, Ni-rich compositions offer promising performance metrics but struggle with accelerated capacity fade and lower thermal stability.

Layered oxide cathodes currently dominate the EV market and NMC-type materials comprised 33% of the total 275 MTon of cathode materials produced in 2017 and is anticipated to grow to over 70% of cathode production by 2025.[43] NMC cathodes are currently being used in Chevy Volt and the BMW i3 vehicles; however, Ni-rich compositions are expected to see wider utilization in next-generation EVs.[55]

1.3.4 $LiNi_{1-x-y}Co_xAl_yO_2$, $x + y < 0.2$ (NCA)

$LiNi_{1-x-y}Co_xAl_yO_2$ (NCA) is another transition metal layered oxide type cathode material that has been of considerable interest for use in EVs, notably the composition of $LiNi_{0.80}Co_{0.15}Al_{0.05}O_2$ finding application in the Tesla Model S and Model 3 vehicles. The development of NCA originated from the idea that a hybridization of $LiNi_{1-x}Co_xO_2$ and $LiNi_{1-x}Al_xO_2$ could have synergistic effects as both materials had been previously reported as having acceptable electrochemical performance.[21] The Ni^{2+} and Co^{3+} cations have a similar function to their use in NMC; however, the addition of electrochemically inactive Al^{3+} now contributes to the structural rigidity and thermal stability of the material during lithium insertion and extraction instead of Mn^{4+}. Since Al^{3+} is inactive, a high fractional component will decrease the available capacity of the material. The Al content in NCA is typically low ($y \leq 0.05$) such that the $Co^{3+/4+}$ redox which is possible on the range of 2.5-4.3V vs. Li^+/Li can compensate for the slight capacity reduction (~5%).[56,57]

$LiNi_{0.80}Co_{0.15}Al_{0.05}O_2$ can deliver 200mAh.g^{-1} on the same voltage range and good cycling stability has been reported. A study by Watanabe *et al.* compared the stability of NCA and LCO cathodes with a 60% DOD condition and it was found that the NCA cathode performed considerably better than LCO, retaining over 90% of their initial capacity after 2500 cycles.[30] Although the performance is promising, considerable research effort is still needed to improve the thermal stability (safety) of the material and the capacity retention (lifetime) when cycling at higher DOD conditions. These are both considered key factors to successful commercialization in next-generation EVs. Many strategies to resolving these issues have been investigated, including a

recent report by Li *et al.* that focused on adjusting the particle morphology to mitigate the capacity fade in $LiNi_{0.88}Co_{0.09}Al_{0.03}O_2$ at higher DOD.[9]

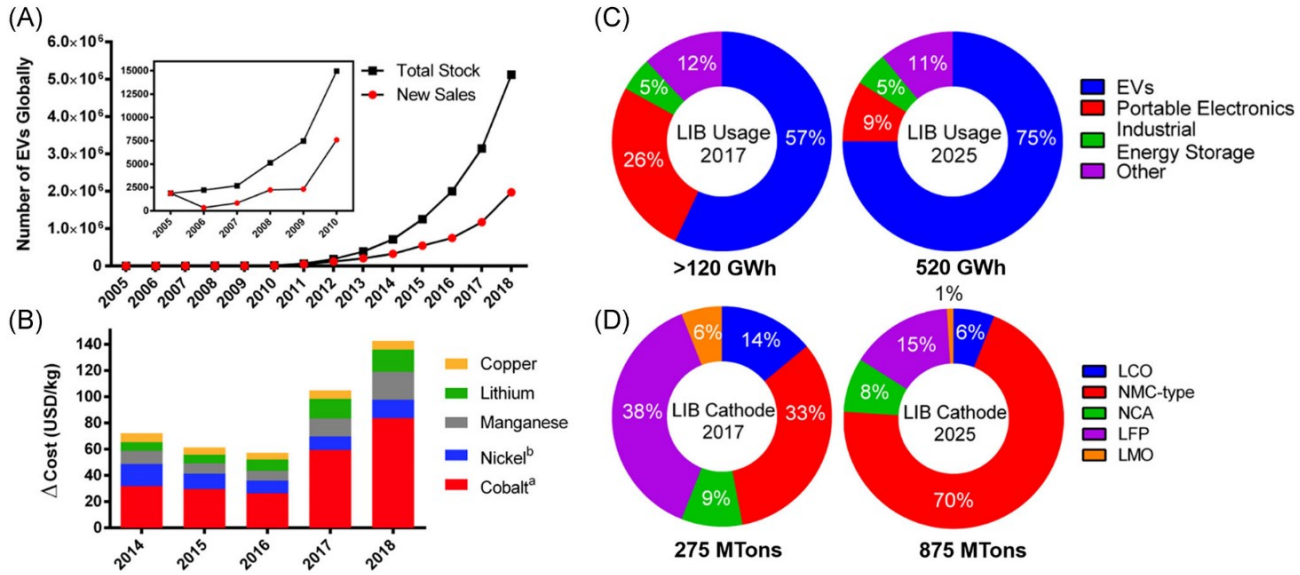

Figure 6 - A, Number of EV sales globally. B, Price of valuable metals in LIBs in 2018 from the US Geological Survey. Projection of LIB market share based on (C) application and (D) cathode composition.[58]

1.3.5 Cation Disordered Rocksalts (DRX)

As advancements to the performance and safety of these conventional battery materials continue to be made, further concerns for their sustainability have emerged with particular focus placed on the over-utilization of cobalt. Olivetti *et al.* describe a conservative scenario based on 36% compound annual growth rate (CAGR) for EVs by 2025, with the assumption that LIB utilization in EVs will comprise 50% NMC622, 35% NMC111, and 15% NMC811 taking into consideration further commercialization of Ni-rich NMC by 2025.[59] An aggressive scenario projecting 10 million EV sales in 2025 (10% all passenger vehicle sales) is also reported, with these scenarios corresponding to 136kt and 330kt of cobalt demand, respectively. The problem arises when comparing the projected supply growth for conservative (180kt) and aggressive

(290kt) scenarios to the demand, clearly illustrating that a cobalt supply deficit is possible if the aggressive scenario is met even with increased use of low-Co cathodes (e.g. NMC622, NMC811) in EVs. As such, it is clear that these low-Co materials are not a complete enough solution and the development of high energy, Co-free materials is needed if EV sales targets are to be met without incurring a supply deficit. Improvements to Ni-rich NMC and NCA cathodes that reduce cobalt content are still necessary as the transition from existing commercial LIBs to Co-free next-generation LIBs will be a gradual process. This section will highlight the advantages of two emerging classes of Co-free cathodes as well as the barriers for their commercialization.

Conventional cathode materials typically possess a well-ordered layered, spinel or olivine type lattice, with particular attention given to layered transition metal oxides with the α-$NaFeO_2$ structure shown in Figure 7b. In contrast, disordered materials have been largely overlooked for use in LIBs. As previously discussed, the Li sites and diffusion channels within ordered materials are separated from the transition metal sublattice and the prevention of intermixing within the lattice is considered critical to achieving a stable electrochemical performance. A major reason that layered NMC or NCA cathodes must contain Ni, Mn, or Co as a main component is due to the fact that these transition metals are among the few that do not shift to Li sites at high degree of delithiation.[60] As disordered structures are based on an intermixed network, they are therefore primarily considered electrochemically inactive or associated with an inactive phase in conventional cathode materials. DRX materials crystallize into a ccp oxygen lattice with lithium and transition metal ions located at octahedral sites in a theoretically random arrangement forming an α-LiFeO2 structure illustrated in Figure 7a. Instead of leading to degradation or an inactive phase, the disordered structure results in lower volumetric change of the lattice during charge and

discharge that is commonly associated with detrimental phase changes that occur in layered oxide cathodes. As Ni, Mn, and Co are no longer required as majority elements, this class of electrodes effectively expands the chemicals available for these next-generation LIBs.[61]

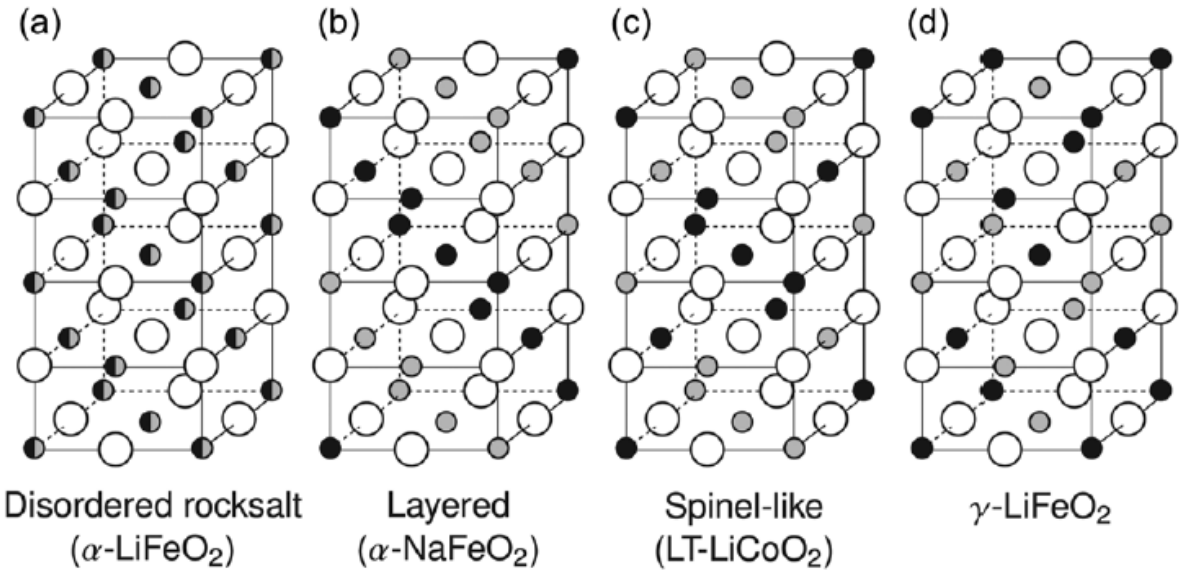

Figure 7 - Common rocksalt-type lithium transition metal oxide crystal structures: (a) the disordered rocksalt a-LiFeO2 structure, (b) the layered a-NaFeO2 structure, (c) the spinel-like low-temperature LiCoO2 structure, (d) the g-LiFeO2 structure. White circles indicate oxygen, small gray/black circles indicate lithium and transition metal sites, respectively.[62]

Experimentally, many compositions have been tested for their propensity to form a DRX material. It was suggested by Urban *et al*.[63] that the physics of disorder is determined by the fill level of the d-orbital of the transition metals, as each fill level has a preferred octahedral distortion. It was found that transition metals with an empty d-orbital (*e.g*. Nb^{5+}, Ti^{4+}) are able to best stabilize the disordered structure despite the possibility of a large difference in ionic radius of the cation species. Numerous DRX compositions have been reported to deliver higher gravimetric capacities than conventional LIB cathodes, including $Li_{2-x}VTiO_4$ (300mAh.g^{-1}),[64] $Li_{1.3}Nb_{0.3}V_{0.4}O_2$ (270mAh.g^{-1}),[65] $Li_{1.2}Ni_{0.33}Ti_{0.33}Mo_{0.133}O_2$ (230mAh.g^{-1}),[66] and $Li_2Mn_{2/3}Nb_{1/3}O_2F$ (300mAh.g^{-1}).[67] The high

capacity of DRX materials is enabled by two main factors. Firstly, the inclusion of high valence transition metal cations allows for a greater fraction of low-valent, redox active transition metals (*e.g.* Ni^{2+}, Mn^{2+}) to exist within the cation sublattice and therefore a greater theoretical capacity available from transition metal redox. Secondly, the charge compensation for Li^+ extraction in DRX cathodes is due not only to the oxidations of transition metal ions but also to the O^{2-}/O_2^{2-} process. Although the reversible oxygen participation to the redox reaction is not unique to DRX cathodes, it is an important factor in attaining the elevated capacities listed above.[68,69] The combination of these two factors allow for enriched lithium content in the cathode leading to an exceptionally high theoretical capacity (>300mAh.g^{-1}) and energy densities approaching 1000 Wh.kg^{-1} on the voltage range of 1.5-5.0 V vs. Li^+/Li.[67,70]

However, despite the promising nature of these materials numerous barriers exist to their commercialization that require further research, including poor rate performance, low cyclability, and low discharge voltage with <250mAh.g^{-1} capacity above 3.0V vs. Li+/Li. Unlike ordered materials with clear Li^+ diffusion channels with at least one face-sharing transition metal ion (1-TM), Li^+ ions in DRX materials can diffuse through pathways with no face-sharing transition metal ions (0-TM) as well. The 1-TM pathways in conventional layered oxides offer high ionic mobility; however, within disordered rock-salts these 1-TM pathways become practically inactive. Li^+ diffusion occurs through a repeated process of hopping from octahedral site to octahedral site within the lattice via an intermediate tetrahedral site (o-t-o diffusion). In the case of 1-TM channels in DRX cathodes the height of this tetrahedron is compressed causing an increased electrostatic repulsion between the transition metal and Li^+ ion, increasing the mean energy barrier required for the hopping process to occur (~500meV). 0-TM channels do not encounter this repulsion and

typically have an energy barrier similar to that of 1-TM channels in layered oxide cathodes (~300meV); however, the fraction of 0-TM channels within DRX materials is often too low to form a percolating network. Due to this issue, Li^+ has a low macroscopic diffusion rate in DRX cathodes leading to poor rate performance of the battery.[71] The cycling instability of DRX cathodes originates from the participation of anionic species in the redox processes for charge compensation. Specifically, at high voltages (>4.5V vs. Li+/Li) oxygen vacancies at the cathode surface are realized through oxygen evolution due to cathode-electrolyte interfacial side reactions. The surface level vacancies are able to migrate towards the bulk and over time form nano-voids within the particle causing rapid capacity fade.[36]

This thesis focuses on the development of a DRX material and the optimization a synthesis methodology to improve cycling performance by mitigating the effects of oxygen loss, and surface modification to improve the rate capability of the cathode.

1.4 Surface Coatings

Surface treatments and modifications have attracted a considerable amount of research attention as a means of improving the electrochemical performance of LIB cathode materials. Many researchers have used surface coatings (e.g. Al_2O_3, $AlPO_4$, SiO_2 or ZrO_2) to assist with structural and thermal stability in layered oxide cathode materials. The numerous coatings all aim to minimize degradation caused from solid-electrolyte interaction through several mechanisms. Primarily this is accomplished by providing a protective barrier layer on the surface of the active material, acting as a scavenger to reduce acidity of non-aqueous electrolytes, or reducing the dissolution of metallic ions within the cathode structure. Surface coatings can also be used to

increase the rate capability of the battery by providing improved ionic or electrical conductivity to the active material, lowering surface contact resistance between particles facilitating faster transport of electrons from the cathode to the current collector.[72–74]

Several strategies exist to apply surface coatings to a positive electrode material including atomic layer deposition (ALD) which provides precise control over the film enabling nanometer thicknesses and uniform surface coverage. ALD is typically used for inorganic, oxide coatings such as alumina or titanium dioxide and can take place with a powdered active material or prepared electrodes as substrate.[75,76] Solvent casting is a technique primarily used for polymer-based coatings such as polyacrylonitrile (PAN) whereby the polymer is dissolved in an organic solvent with the active material precursor and forms a composite material upon evaporation of the solvent.[77,78]

1.5 Thesis Framework

Chapter 1 provided detailed information on the fundamentals of LIB operation, including the basic working principles and individual components as well as a brief discussion on common mechanisms of degradation. Examples of conventional and emerging cathode compositions for LIBs were examined, focusing on the advantages and disadvantages of each along with the complex socioeconomic challenges that are potential barriers to their future use.

Chapter 2 of this thesis provides detailed information on the experimental scope of the project including the processes for synthesis, electrode preparation, coin-cell fabrication and the operation of techniques frequently used for LIB characterization. The physical characterization

methodologies of scanning electron microscopy (SEM), thermogravimetric analysis (TGA), and powder x-ray diffraction (XRD) will be discussed as well as electrochemical characterization through electrochemical impedance spectroscopy (EIS), and cycling techniques used for determination of charge/discharge rate capability, and long-term cycling stability.

Chapter 3 describes the development of a performance-optimized $Li_{1.25}Mn_{0.5}Nb_{0.25}O_2$ cation-disordered rock-salt cathode material. The effects of the variation in synthesis methodology including sintering temperature, time, and lithium content will be discussed alongside variations in electrode preparation methodology. Surface modifications/treatments used for this study are elucidated including the use of a Li_2O-B_2O_3 composite and ALD of alumina (Al_2O_3). Physical characterization of the materials/electrodes will be included where applicable. Furthermore, a comparative analysis of the electrochemical performance of the samples including reversible capacity, cycling stability, and rate capability is performed.

Chapter 4 broadens the scope of this thesis by providing considerations for extensions of the work reported and directions for future research. Limitations of the study will be discussed as well. Finally, Chapter 5 concludes this thesis with a summary of results and a brief discussion on the outlook of this material for commercialization.

2. Experimental

2.1 Experimental Scope of Research

As mentioned, the motivation for this research was to investigate the disordered rocksalt class of positive electrode materials for lithium-ion batteries and to study the effects of a modified synthesis methodology and surface coating on the electrochemical performance of the battery. The cathode active materials were prepared using a multi-phase synthesis technique and formed into electrodes through a slurry coating process, both of which will be detailed in this chapter. The select coating films were applied to the oxide powders after synthesis or the prepared electrode surface through atomic layer deposition or solvent casting methods. Half-cell coin-cells were prepared with the synthesized material and used for measuring the electrochemical performance. During each step of synthesis, the morphology and structure of the materials were characterized through several techniques including scanning electron microscopy (SEM) and powder x-ray diffraction (XRD). Electrochemical data including first cycle deliverable capacity and coulombic efficiency (CE) were also measured for each material, while cycling performance and rate capability were studied only for select cells. This section will focus on the experimental procedures used for synthesis and characterization of all materials covered within the scope of this project.

2.2 Precursor Materials

The synthesis of precursor materials for lithium-ion battery cathodes is typically accomplished through one of two methods.[79] The first being the co-precipitation of a mixed transition metal hydroxide or carbonate that acts as a template structure for the active material particles. The precursor is then mixed with a lithium source, typically lithium hydroxide (LiOH) or lithium carbonate (Li_2CO_3) in the desired stoichiometric ratio and then heat-treated. The

precipitation process is sensitive to the temperature, pH, and mixing rate leading to several studies focused on optimizing the yield and quality of the precursors prepared through this process.[80,81] Co-precipitation has been reported over the last decade as a synthesis method for many well commercialized materials (*e.g.* NMC111).[82]

The second method is the mechanochemical grinding of oxides, carbonates, and hydroxides of the desired elements (*i.e.* Li, Ni, Mn, Al, Co, Nb, *etc.*) in stoichiometric proportion. The homogenously mixed precursor is then heat-treated to yield the final positive electrode product. To compensate for the potential loss of lithium during high temperature sintering, the addition of excess lithium oxide is sometimes added to the mixed powder before heat treatment.[67]

In this project we utilized precursor materials prepared through both solid-state and co-precipitation methods. 500g of $Mn_{0.66}Nb_{0.33}CO_3$ prepared by co-precipitation was obtained from Hunan Zoomwe New Energy Science & Technology Co., LTD and used as a precursor material throughout this study. Mechanochemical grinding was also done to prepare precursor materials with stoichiometric amounts of Mn_2O_3 (Sigma-Aldrich, 99.0%), Nb_2O_5 (Sigma-Aldrich, 99.9%), NiO (Sigma-Aldrich, 99.9%) and a lithium source of Li_2CO_3 (Sigma-Aldrich, 99.0%), LiOH (Sigma-Aldrich, 98.0%), or LiF (Sigma-Aldrich, 99.9%) dependent on the desired composition.

2.3 Solid-State Synthesis

2.3.1 Mechanical Pre-treatment

The preparation of the precursor materials falls into the pre-sintering treatment phase of the synthesis methodology. Various techniques were used during this phase in an effort to optimize the performance of the prepared material after sintering. Each technique will be described in detail below.

Manual Grinding

As prepared $Mn_{0.66}Nb_{0.33}CO_3$ was mixed with lithium source (*e.g.* Li_2CO_3, LiOH) and ground using mortar and pestle for 15-20 minutes until the mixture was homogenous (*i.e.* no observable white powder from lithium source). This method was also examined for the mechanochemical preparation of the precursor from oxides.

Ball-Milling (Dry)

A Nanjing University QM-WX04 planetary mixer was used for the mechanochemical preparation of the precursor material. Manganese (III) oxide (Mn_2O_3) or nickel (II) oxide (NiO) was added with niobium (V) oxide (Nb_2O_5) to a stainless-steel container along with either lithium carbonate (Li_2CO_3), lithium hydroxide (LiOH), or lithium fluoride (LIF) in desired proportions. Between 5-15 stainless-steel or ceramic balls (0.5cm diameter) were added to the container before being sealed and placed into the mixer. The powders were milled at 200rpm, 600rpm, or 1200rpm for 5, 10, or 24 hours.

Ball-Milling (Wet)

In some cases, a small amount of solvent was added to the dry powders to facilitate a more homogenous mixing process. For this purpose, acetone or de-ionized water was added to the oxide powder with a ratio of 5 ml (solvent) : 1 g (powder). The slurry was then milled at 100rpm, 200rpm, and 600rpm for 1, 2, or 5 hours. After milling, the sample was dried at 80°C for 24 hours under vacuum.

2.3.2 High-Temperature synthesis

The formation of the disordered rocksalt material for use as a lithium-ion battery cathode requires lithiation of the precursor powders through a high temperature sintering process that enables a solid-state reaction. A sample of the two-phase reaction for the formation of the $Li_{1.25}Mn_{0.5}Nb_{0.25}O_2$ is shown in Eqn 2.1 and 2.2.

$$5Li_2CO_3 + 2Mn_2O_3 + Nb_2O_5 \rightarrow 4LiMn^{3+}O_2 + 2LiNb^{5+}O_3 + 2Li_2CO_3 + 3CO_2 \Uparrow \quad (2.1)$$

$$4LiMn^{3+}O_2 + 2LiNb^{5+}O_3 + 2Li_2CO_3 \rightarrow 8Li_{1.25}Mn_{0.5}Nb_{0.25}O_2 + 2CO_2 \Uparrow \quad (2.2)$$

The sintering temperatures for this study exceed the levels required for fusion and decomposition of the lithium source, which is ~720°C for Li_2CO_3 and ~470°C for LiOH. The specific advantages of using LiOH for low-temperature synthesis of disordered rocksalts were not investigated in this thesis.

The preparation of single crystal particles was achieved through two different methods. The first of which is well reported for synthesis of layered oxide type positive electrode materials (NMC532, NMC622, NCA) and required an elevated sintering temperature (≥900ºC) and longer sintering time to allow for increased growth of the primary particles.[9,38,83] A lithium-to-transition metal mass ratio (Li/TM) ~1.20 is needed for this process as excess lithium carbonate has been reported to increase the particle grain size as well as account for the loss of lithium due to the elevated temperature. Flux-mediated synthesis was also used as a method to prepare single crystals of the disordered rocksalt material.[84,85] For this method, the addition of a KCl or LiCl non-oxidizing salt in considerable excess to the active material powder has been reported to assist in homogenous growth resulting in single crystal micron-sized particles.[86–88]

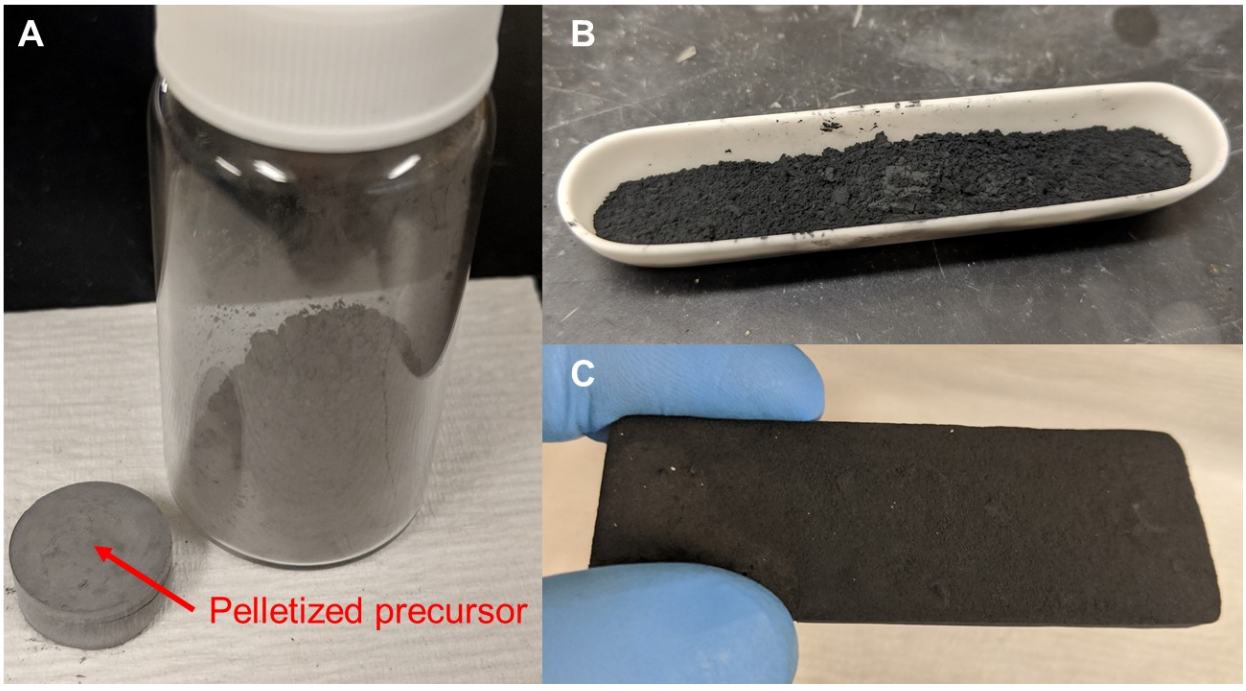

Figure 8 - Active material powder (A) before sintering (left: pelletized precursor, right: powder precursor); (B) after sintering (polycrystalline); (C) after sintering (single crystal)

2-10g samples of the milled precursor powders were added to an alumina heating crucible and tapped down with a stainless-steel scoopula to ensure a loose packing. For flux-mediated synthesis, KCl was mixed with the transition metal oxides in a 5:1 mass ratio and manually ground in a mortar and pestle for 10-20 min until homogenous before being added to the crucible. Some samples were pressed into a compact pellet using a powder die press prior to transfer to the alumina crucible (Figure 8A). Sample pelletization was investigated for improved efficiency during sintering, requiring lower time at a higher temperature. The crucibles were then transferred to either a Lindberg TF55035A-1 tube furnace or an Across GCF1100 atmosphere furnace for heat treatment. The heating and cooling rate, dwell temperature, and dwell time could be programmed for both furnaces. The heating and cooling rates were programmed to be the same at $10^{o}C.min^{-1}$ with a max dwell temperature of 800-1000^{o}C and a dwell time of 6h, 12h, 24h, or 36h. A constant flow of argon or nitrogen gas was used to maintain an inert environment during the sintering process and prevent unwanted oxidation of the material. For the carbonate precursor prepared by co-precipitation ($Mn_{0.66}Nb_{0.33}CO_3$), an additional heat treatment at 550^{o}C for 6h under constant oxygen gas flow was done before the high temperature sintering. The samples were removed from the furnace after cooling to 100^{o}C and transferred to a glass scintillation vial for post-sintering treatment.

2.3.3 Post-Sintering Treatment

The material resulting from the sintering process at lower temperatures (<900^{o}C) or without the molten salt flux was a loose powder (Figure 8B) that was then manually ground using a mortar and pestle for 5-10 min to break up any large agglomerates. The samples prepared with a KCl salt flux formed into a solid “brick-like” block (Figure 8C) after sintering that was first

manually ground using a mortar and pestle until a coarse powder was formed, and then ball-milled in the planetary mixer at 1200rpm for 10 min to achieve a loose powder without any agglomerates. An additional washing step was required for the single crystal samples after ball-milling in order to remove any excess Li_2CO_3 or KCl that might remain on the surface. The loose powder was added to a 50mL beaker with ~20mL of DI water and stirred at 200rpm for 4h. The solution was transferred to a 50mL conical tube and centrifuged at 8000rpm for 5min to separate the powder before decanting and drying the powder at 80ºC for 24h. Finally, the dried material was then manually ground for another 5-10 min to form a homogenous powder. The powders were then stored in an 80ºC oven under vacuum to prevent the absorption of any moisture into the structure which could negatively impact the performance of the electrodes.

2.4 Electrode Preparation

The preparation methods for lithium-ion battery electrodes have been attracting more research attention due to the potential benefit that higher active material loadings have on the volumetric energy density of the battery.[89] The electrode microstructure is a direct consequence of the fabrication method, which is a series of complex individual steps that influence each other and require a high degree of quality control. Conventionally electrodes are prepared by dissolving the powder active material with a binding agent (*e.g.* polyvinylidene fluoride, polytetrafluoroethylene) and conductive additive (*e.g.* carbon black) into of an organic solvent (*e.g.* 1-methyl-2-pyrrolidone) mixing until homogeneous to form an electrode slurry. This slurry is then coated onto a thin, metallic current collector and the solvent is evaporated. This process was promoted and optimized by Marks' *et al.* in a study examining a large number of coin-cells and the impact that

parameters such as active material to binder/conductive additive ratio, coating thickness, drying temperature and calendar pressure have on the electrochemical performance of the battery.[90]

Recently, a "binder-free" electrode preparation method was proposed by Park *et al.* that utilizes single-walled carbon nanotubes (SWCNT) to form an electrically conductive segregated nanocomposite.[91] The advantage of this material is the ability to achieve a thicker electrode layer without structural collapse or losing adhesion to the metallic current collector which are problems of the preparation method described by Marks *et al.* Electrodes are prepared in this way by mixing an aqueous dispersion of SWCNT (~0.2 wt%) with the powder active material until uniform and coating the composite onto a metallic current collector. Stable electrode layers as thick as 800μm with a high electrical conductivity (10^4 $S.m^{-1}$) and areal capacity of 30$mAh.cm^{-2}$ have been reported. One limitation of this method is the necessity for particle size to be larger than the length of the nanotube filler, as the excluded volume of the particles tends to cause segregation of the nanocomposite.

For this thesis, synthesized active material was fabricated into positive electrodes for electrochemical testing through three different methods including both of the works of Marks *et al* and Park *et al*.

Electrode Preparation I (E1) – PVDF, Carbon black, NMP

Electrodes were formed in a mass ratio of 90:5:5 of active material, poly(vinylidene fluoride) (PVDF) (Sigma-Aldrich), and Super-P carbon black (Alfa Aesar, 99%). Samples were prepared

with a total mass of 1-2g and manually mixed in a mortar and pestle with 1-methyl-2-pyrrolidone (NMP) (Sigma-Aldrich, 99% anhydrous). The amount of NMP added was adjusted per sample depending on the resultant viscosity of the slurry; a mass ratio of ~1.5:1 NMP to active material was typically utilized. The slurry was mixed until homogenous and smooth to ensure all agglomerates had been separated. A sheet of aluminum (~150μm thick) was cut to 20cm x 15cm and flattened to a glass plate using a small amount of ethanol. The slurry was then poured (assisted by scoopula) into a uniform line on the top of the aluminum sheet and an angled metal blade (200μm gap) was pulled across the length of the sheet. The electrode was then transferred to an evaporating oven and dried at 100ºC for 3 hours. Electrodes were punched into circles using a 15mm diameter manual die cutter and stored at 100ºC under vacuum for 24h to remove any excess moisture.

Electrode Preparation II (E2) – PTFE, Carbon black, EtOH

The second method to prepare electrodes from the synthesized active material was used when precise control over the specific mass loading was required (*i.e.* specific discharge capacity measurements).[92] The electrodes were prepared by adding the active material, carbon black (Ketjenblack, Lion Specialty Chemical Co., Japan), and polytetrafluoroethylene (PTFE) acetylene black in a mass ratio of 80:10:10. Samples were prepared with a total mass of ~10mg and mixed with ~5ml of ethanol (EtOH). The samples were hand ground in mortar and pestle until the ethanol was completely evaporated and a thin film formed. The film was then pressed into a 15mm diameter stainless steel mesh (~10,00kPa) and dried at 100ºC for 24h under vacuum.

Electrode Preparation III (E3) – SWCNT, EtOH

The final method follows the work of Park *et al.* to prepare a segregated nanocomposite electrode with higher active material loading. 1-2g active material powder and 20ml DI water were added to the planetary mixer and ball-milled at 500rpm for 10min to remove any large agglomerates. The solution was placed in a 50ml conical tube and centrifuged at 8000rpm for 5min, followed by decanting off the water and drying the active material in an evaporation oven at 100ºC for 12h. The active material was then mixed with an aqueous dispersion of SWCNT (0.2 wt% SWCNT in water, 0.2 wt% polyvinylpyrrolidone (PVP) as stabilizer) (Tuball, OCSiAl) in a mass ratio of 99:1 active material to SWCNT. 2ml of EtOH was added to the mixture and transferred to a 20ml glass scintillation vial. The mixture was placed in a sonicator bath for 10min to prevent any agglomeration and then transferred to the planetary mixer (no milling balls were added) to homogenize the slurry at 2000rpm for 10min. The slurry was then poured (assisted by scoopula) onto an aluminum sheet and an angled blade (200µm) was dragged across the surface as in method E1. The electrodes were transferred to an evaporation oven and dried at 100ºC for 3h. The electrodes were then punched into circles with a 15mm diameter manual die cutter. Finally, the punched electrodes were wrapped in Al-foil to prevent deformation and heat-treated at 350ºC for 30min to remove any remaining PVP in the structure.

2.5 Coin-Cell Fabrication

Electrochemical performance of the positive electrode material was determined using the laboratory coin-cell form factor that was fabricated following the guidelines indicated in the recent work by Murray *et al*.[93] The 15mm electrode disks were weighed using a microbalance with

0.01mg resolution (Sartorius SECURA225D1S). Each electrode had a mass between 10-15mg including the ~7mg mass of the Al-foil leaving 3-8mg of electrode material per disk. The remaining mass was then multiplied by the fractional component of active material in the slurry (*e.g.* 0.9 for 90:5:5 compositions). It was critical to have a high degree of accuracy for the active material mass as it was used in the determination of the current applied during charge and discharge as well as the gravimetric capacity calculation.

In addition to the punched working electrodes, coin-cell assembly required several other components including a counter electrode, separator, spacer, casing, and electrolyte. For the majority of materials discussed in this thesis the electrolyte solution used for coin-cells was LP57 (Gotion) containing 1M lithium hexafluorophosphate (LiPF6) dissolved in mixed ethylene carbonate (EC) and ethyl methyl carbonate (EMC) at a mass ratio of 3:7 and vinylene carbonate (VC). Two different types of separator were used in all coin-cells prepared for this thesis, either a polypropylene Celgard #2300 (Celgard LLC) or blown microfiber (BMF) separator (3M). A 16mm diameter piece of lithium metal was used as the reference/counter electrode.

Coin-cells were all assembled in an argon filled glovebox (<1ppm O_2, <0.1ppm H_2O) as the lithium metal counter electrode is highly reactive with both oxygen and water. Furthermore, high moisture content causes decomposition of the organic electrolyte leading to lower performance of the cell which was avoided for this project.[94] A CR2032 sized stainless-steel coin-cell casing was used with dimensions of 20mm diameter and 3.2mm height. Prior to assembly the casings were washed by sonication with EtOH for 5h; EtOH was then removed and the casings were dried at 100^{o}C for 4h under vacuum.

Assembly involved stacking of components as illustrated in Figure 9 except for the use of a different negative electrode. The positive electrode was placed in the center of the large casing and 40µl of electrolyte was dropped using a 20-200µl micro-pipettor (VWR International, LLC). An 18mm diameter separator disk is then placed on the electrode ensuring the electrolyte fully wets the separator. An additional 40-60 µl of electrolyte was then dropped onto the top of the separator. If Celgard 2300 separator was being used, a second 18mm diameter separator disk was placed directly on the first, ensuring they are centered with each other such that there was complete overlap. The 16mm diameter lithium metal counter electrode was first aligned with the 16mm stainless steel spacer and pressed with a Teflon block to ensure good contact. The counter electrode and spacer were then centered with the working electrode and placed on top of the separator layer. Finally, a stainless-steel spring was stacked on the spacer and capped with another casing. The stack was then sealed in a hydraulic crimper (MTI, MSK-110) with pressure of 850psi. The sealed coin-cells were then ready for electrochemical testing.

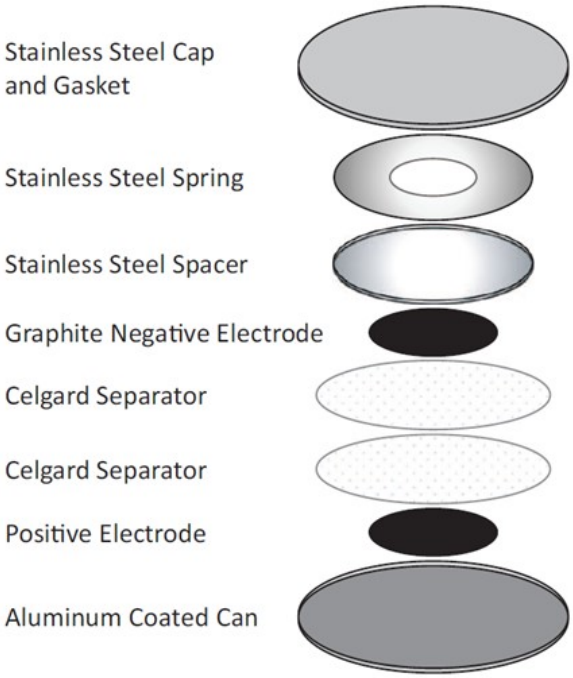

Figure 9 - Schematic of coin-cell assembly.[93]

2.6 Surface Coating

2.6.1 Coating Selection

As mentioned, surface modifications and coatings have attracted considerable attention as a strategy to improving performance of cathode materials for lithium-ion batteries, particularly for Co-free materials. Inorganic surface coatings (Al_2O_3, $AlPO_4$, and TiO_2) are the most commonly used for cycling stability and lifetime improvements, namely attributed to their ability to scavenge hydrofluoric acid (HF) generated from electrolyte decomposition or acting as a physical barrier between electrolyte and particle surface.[95–97] A recent report by Hall *et al.* suggested that the Al_2O_3 cathode coating reacts with the electrolyte, specifically LiPF6, forming lithium difluorophosphate ($LiPO_2F_2$) which is an chemical commonly added to electrolytes in order to increase the cycling performance and lifetime of lithium-ion cells.[98]

Several studies have been reported on the use of a lithium boron-oxide based material for thin-film solid electrolyte due to its high ionic and electrical conductivity.[99–101] These properties make it an ideal candidate for surface coating to improve the rate capability and stabilize the surface electrolyte interactions. The infusion of a solid electrolyte (Li_3PO_4) into the grain boundaries of a LIB cathode material has been recently reported by Yan *et al.*[102] This work reported the increased lithium diffusion speed and suppression of unwanted solid-electrolyte reactions that are responsible for the loss of oxygen and dissolution of active material. Du *et al.*[103] made use of a lithium boron-oxide glass (LBO-glass) for surface coating on a $LiNi_{0.5}Mn_{1.5}O_4$ cathode to the effect of increasing capacity retention and discharge rate capability of the battery.

Another material that has been used as a coating for lithium-ion battery cathodes is the polymer polyacrylonitrile (PAN). Lin *et al.* demonstrated the positive effects that a cyclized PAN surface coating on $LiNi_{0.5}Mn_{1.5}O_4$ could have on the rate capability and cycling stability of the cathode.[78] This thesis investigates the effects of three different coatings within the scope of those previously discussed. The fabrication methodologies for each coating are detailed below.

2.6.2 Al_2O_3 Coating

The coating of a thin layer of Al_2O_3 on the electrode surface was performed using an ALD reactor (Thermal Gemstar 6XT, Arradiance, LLC, USA) at 115 °C with trimethylaluminum (TMA) used as precursor and H_2O as oxidizer. The precursors were purged for a time of 21 ms with coating thickness being controlled by the number of deposition cycles. Ten cycles were used for this work. Both active material powder and as prepared electrodes were used as the substrate

in different tests; however, the latter was used more frequently and will be discussed for the remainder of this thesis unless otherwise noted.

2.6.3 $2Li_2O$-B_2O_3 Coating

A stoichiometric amount of lithium hydroxide (LiOH), lithium carbonate (Li_2CO_3) and boric acid (H_3BO_3) were combined with the synthesized active material and homogenously mixed in deionized water (1:3 solid to liquid ratio) using the planetary mixer at 800rpm for 15min. The solution was transferred to an evaporation oven at 200°C until dried. The remaining powder was then placed in an alumina heating crucible and transferred into a Lindberg tube furnace to be heat-treated at 600°C for 10h with constant argon gas flow. The $2Li_2O$-B_2O_3 coating was fabricated as 2 wt% of the active material mass, with typical sample having 1g active material, 0.004g LiOH, 0.0166g Li_2CO_3, and 0.0035g H_3BO_3.

2.6.4 PAN Coating

Formation of the PAN coating follows the experimental methods described by Hassan *et al.*[77] and Lin *et al.*[78] 1g of active material and 0.01g PAN (Mw = 150,000 g mol^{-1}) were dissolved into 5-10ml N, N-dimethylformamide (DMF) and stirred constantly at 300rpm at 100°C until the solvent was fully evaporated. The remaining powder was placed in an alumina heating crucible and transferred into an Across atmosphere furnace to be heat-treated at 400°C for 1h in air yielding the coated material.

2.7 Characterization Methods

2.7.1 Scanning Electron Microscopy (SEM)

SEM is a useful technique for characterizing the surface morphology, particle size distribution, and can be coupled with energy dispersive x-ray spectroscopy (EDX) to determine elemental composition. SEM is used for its capability to obtain high resolution images of the three-dimensional surface structure (topography) for a wide range of materials and magnifications. The desired measurement area is probed with a highly focused electron beam that is moved across the sample in a raster to form an image. The different interactions between the incident electrons and the sample volume are measured by a detector specific to the desired mode of the SEM. Low-energy (~50eV) secondary electrons have a small mean free path in a solid and their detection is limited to the emission from the sample surface. If the electron is emitted from a core orbital level then a higher energy electron can drop to the vacant position and release energy in the form of an x-ray photon in the process. This characteristic x-ray can be detected, providing information on the atomic composition of the sample. Higher energy back-scattered electrons (BSE) result from the direct collision of the electron beam with the nuclei of atoms in the sample. The BSE count is directly related to the atomic mass of the atoms in the sample, thus giving heavier elements a brighter appearance than lighter elements in an SEM image and giving information about the sample composition.[104]

The electron gun generates electrons with an energy in the range of 0.1-30 keV that is sent through a series of lenses to accelerate and focus the beam to a spot size of ~10nm on the specimen.

The Zeiss UltraPlus SEM at the University of Waterloo Advanced Technology Laboratory was used for the SEM characterization of all samples reported in this thesis. The SEM required a

4-component set-up including a water-cooling system, nitrogen gas tanks, computer control panel, and the SEM machine itself. Each of these was critical in the continued operation of the device. Specimens were prepared by mixing 50-100mg of powdered sample with 5ml EtOH with a mortar and pestle for 5min. 10-20µl of the solution was then dropped onto a stainless-steel SEM stub and dried at 25ºC for 25min until all solvent had evaporated. A light flow of nitrogen gas was then applied to the sample to prevent contamination. For low conductivity samples a thin layer of gold was sputtered onto the surface to prevent electron charging during SEM operation and the formation of unwanted artifacts in the images.

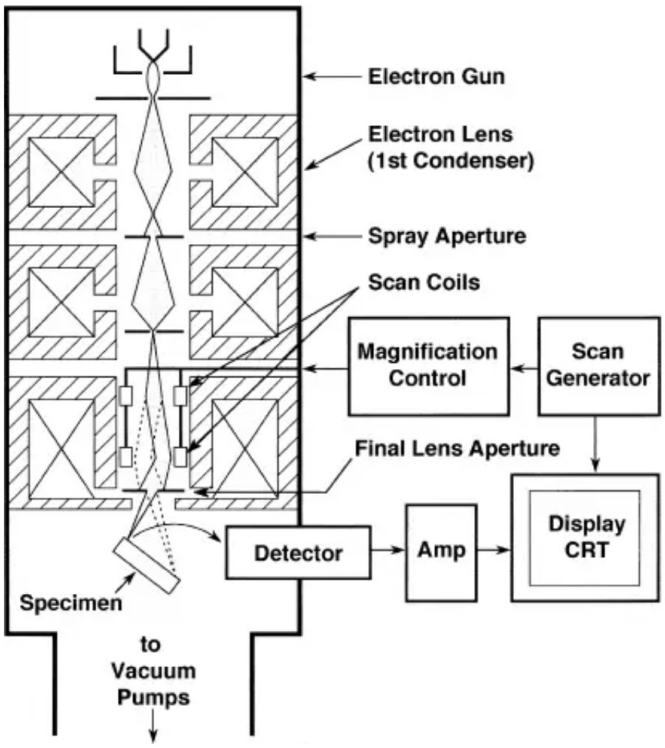

Figure 10 - Schematic of the SEM column containing electron gun, condenser, aperture, scanning coils, specimen stage, and detector control flow.[104]

2.7.2 Powder X-Ray Diffraction (XRD)

XRD is another useful characterization technique to determine the crystal structure or lattice spacing of a sample. The technique is based on the x-ray, a type of electromagnetic radiation which results in an absorption or scattering event when interacting with a material. The scattering event can be broken into an elastic and inelastic component which is used to probe the structure of the material and can be quantified using Eqn 2.3.

$$I_f = \frac{I_0 K}{r^2}\left(\frac{1+\cos^2 2\theta}{2}\right) \tag{2.3}$$

$$\lambda = 2d\sin\theta \tag{2.4}$$

In this case I_0 is the intensity of the incident beam, I_f is the intensity of the scattered beam, r is the distance from the event which I_f is measured, and θ is the Bragg angle. When the wavelength (λ) of the x-ray matches the spacing between planes in the crystal the resulting scattering event has a much higher intensity (constructive interference). The condition for this constructive interference to occur is known as the Bragg law (Eqn 2.4) and illustrated in Figure 11. The atomic plane spacings (d) within the lattice can now be determined using Bragg's law by measuring the angle of the diffracted x-ray beam.

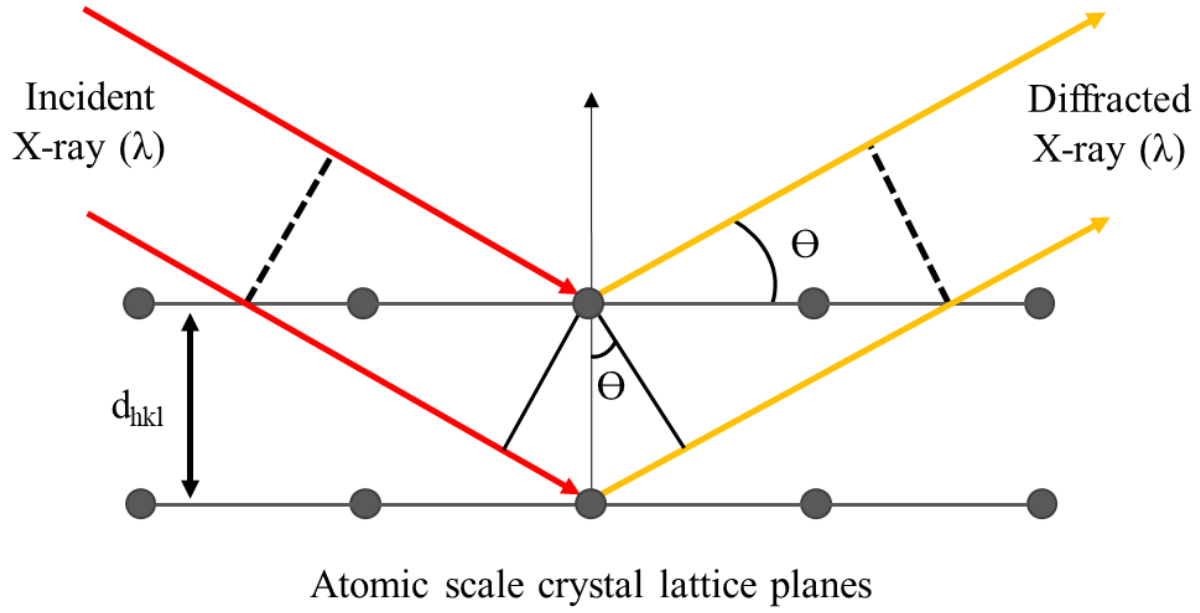

Figure 11 - Schematic of Bragg diffraction in crystal lattice planes.

For crystalline samples, the allowed spacings that result in the constructive interference needed to satisfy Bragg's law are well known to be associated with specific crystal structures. Comparative analysis of the measured spacings and experimental results recorded in a database such as the Crystallography Open Database by the Department of Chemistry at the University of Cambridge can then assist in the identification of the sample.

This technique was carried out using a Rigaku MiniFlex 600 diffractometer and the resulting diffraction spectra were analysed using PDXL Ver 1.8.0.3 and MAUD Ver 2.92 software. The diffractometer produces an x-ray source through the interaction between a high energy electron beam striking a copper plate to produce x-rays that are then focused onto the sample using a collimator. The sample stage was then rotated through a set range of angles (2Θ) and the intensity of the x-ray scattered off the sample at each step (angle) on the range was measured at a detector. The scattered intensity was plotted against the angle (2Θ) generate a diffraction spectrum which

was analyzed to identify the crystalline components of the sample. 50-100mg of powdered sample was pressed onto a quartz glass sample holder and placed in the diffractometer. The sample was measured on the 2Θ range of 5-90º with a step size of 0.02 and a speed of 2.0 º/min.

2.7.3 Thermal Stability

Thermogravimetric analysis (TGA) is a quantitative analytical technique that gives insight to the structural nature of the sample. TGA is used for lithium-ion battery electrode materials to determine their thermal stability, often paired with accelerating rate calorimetry (ARC) to measure the self-heating rate of cathode materials and their stability at elevated temperatures.[105] TGA monitors the mass of a sample material across a specific temperature range (up to 1600ºC) due to decomposition of the material. TGA takes place under an inert environment (*e.g.* argon, nitrogen) to prevent any unwanted reactions between the sample and environment which could impact the results.[106] ARC utilizes a confined adiabatic environment (*i.e.* energy is only transferred to surroundings as work) to analyze the exothermic properties of a sample. This is particularly useful for determining the safety of a lithium-ion battery cathode, as the only increase in temperature will be due to self-heating allowing its rate to be measured for a given temperature range and analysis of the thermal runaway potential of a material (Figure 12).[107,108]

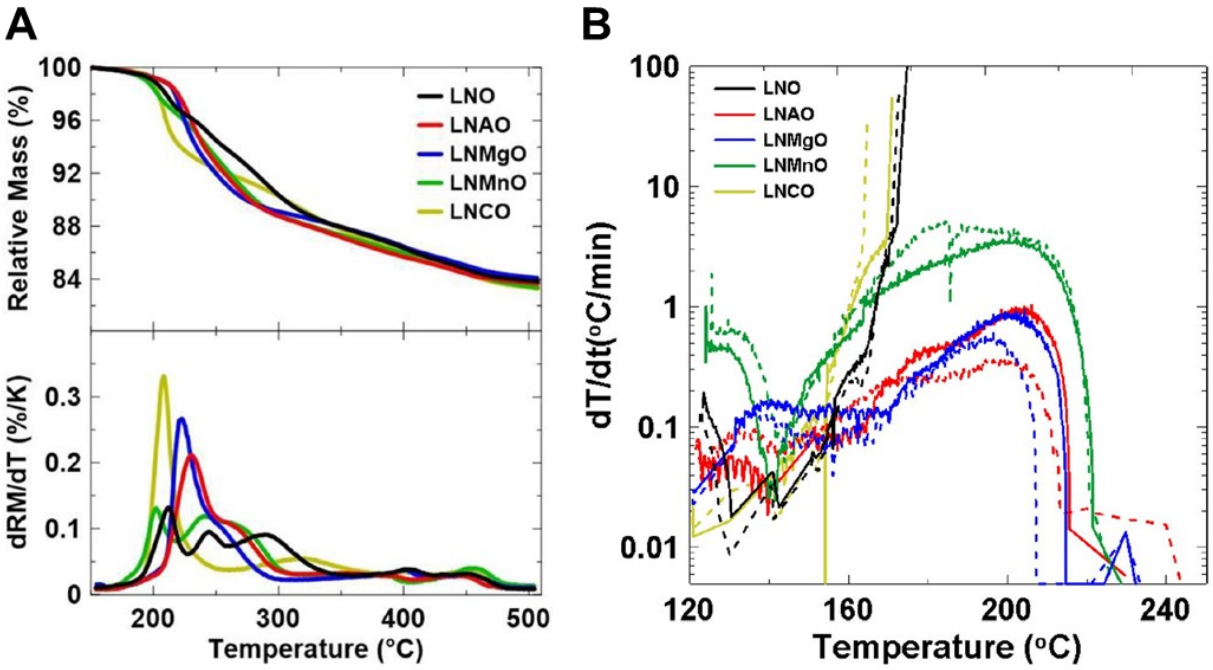

Figure 12 - Study of the thermal properties for $LiNi_{1-x}M_xO_2$ (M=Al, Mg, Mn, Co). A: Normalized TGA (top panel), derivative of the normalized mass loss vs. T (bottom panel). B: ARC for 120°C-250°C showing self-heating rate as a function of temperature.[108]

2.7.4 Electrochemical Impedance Spectroscopy (EIS)

The concept of electrical resistance is well known as the ability of an element in a circuit to limit the flow of current. It can be quantified as the ratio between the voltage (V) and current (I), commonly known as Ohm's law (Eqn 2.5). Although this concept is useful for ideal single circuit elements, a complex electrochemical system requires looking at the complete picture including non-idealities.

$$R = \frac{V}{I} \tag{2.5}$$

Impedance is the measure of the resistance to the flow of electric current in a circuit, similar to resistance; however, unlike resistance the impedance of a system applies in the case when AC current is used rather than DC current. To measure the impedance of a system, an AC potential is

applied to a cell and the current passing through the cell is monitored. The impedance of an electrochemical cell is a function of the frequency of the applied potential with a real and imaginary component (Eqn 2.6) that are plotted against one another in a Nyquist plot.[109]

$$Z(\omega) = \frac{V}{I} = Z_0(cos\phi + jsin\phi) \quad (2.6)$$

In a Nyquist diagram (Figure 13), the negative value of the imaginary component of the the impedance (- im Z) is plotted versus the the real component of the impedance (re Z). Analysis of a Nyquist plot can yield information about the contact, bulk, mass transfer, and charge transfer resistances of a cell and give insight into the degradation of the electrochemical performance without need for destructive testing. The x-intercept at the lowest re Z value is the ohmic resistance of the entire system (bulk resistance), the second semi-circle component of the plot, starting at higher re Z value, is a measure of the electrode-electrolyte interface resistance (charge transfer). The low frequency character of the Nyquist plot is known as the Warburg diffusion impedance and corresponds to the resistance caused by particle diffusion (mass transfer).[110]

For this project, a Gamry Potentiostat was used for EIS and open-circuit voltage (OCV) measurements on coin-cell samples after 1 and 50-100 cycles to compare different mechanisms of impedance growth occurring within the cells.

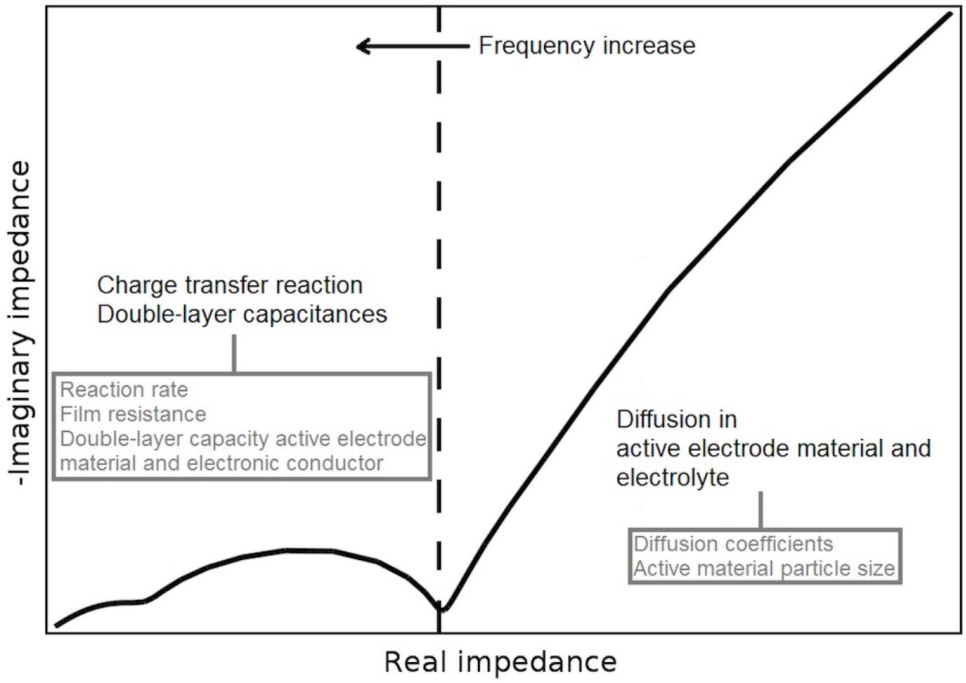

Figure 13 - Sample Nyquist plot describing the character of each region in relation to resistance mechanisms in an electrochemical cell.[110]

2.7.5 Electrochemical Cell Performance

The electrochemical performance of all coin-cell samples fabricated as described in Section 2.5 was measured using a Neware Battery Testing System (BTS4000). Samples were placed into either a built-in coin-cell holder on the BTS4000 instrument, or a holder in a neighboring temperature-controlled chamber attached to the BTS4000. The temperature-controlled chamber was used to maintain a desired temperature of 25°C or 40°C for the coin-cells throughout the duration of testing. A series of cycling profiles were generated using the Neware Battery Testing Software that charged and discharged the coin-cells under specified conditions. Numerous cycling profiles were generated to test different aspects of battery performance, each of which included a protocol of many different steps and conditions. Galvanostatic (constant current) cycling applies a constant current to the samples, and charges or discharges them to a specified cut-off voltage. Potentiostatic (constant voltage) cycling is the opposite, maintaining a constant voltage across the

cell until a specific current is reached. Both of these processes are used frequently in conventional cycling profiles. Once the current and voltage of the coin-cell during the cycling test were recorded at a specified data collection rate, the data was then processed and analyzed in the form of a voltage vs. capacity curve (V vs. Q). Differential voltage (dV/dQ vs. V), and differential capacity (dQ/dV vs. Q) curves are also commonly investigated for the insight they can provide to the phase transitions occurring within the electrode material during the cycling process.[111–113]

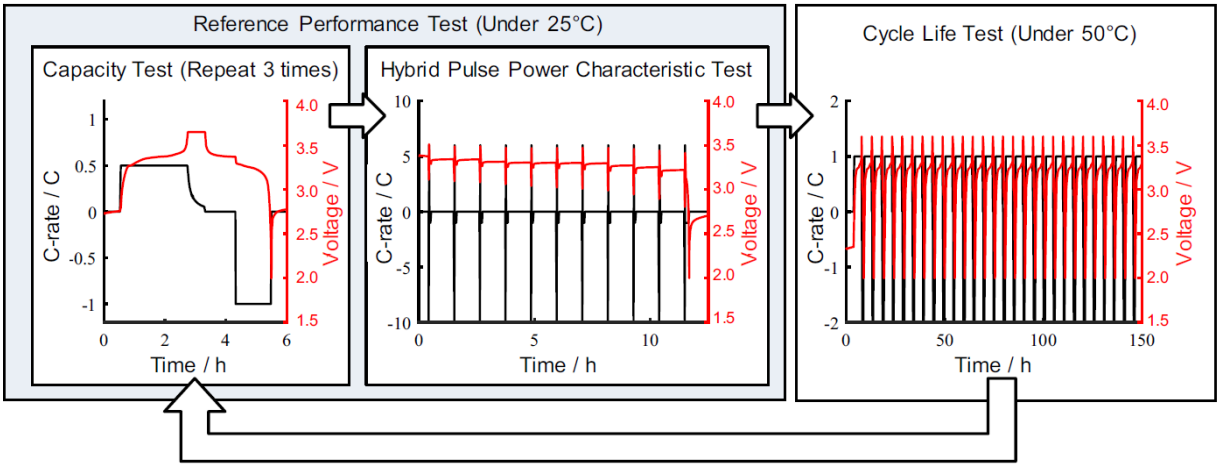

Figure 14 - Example of cycle life analysis for lithium-ion battery including repeated use of reference performance test.[114]

The V vs. Q curve provided a considerable amount of information about the electrochemical performance of a coin-cell depending on the cycling protocol used for the test. Initial performance of a battery was typically measured using a reference performance test (RPT), where a lower current/C-rate was used to ensure complete (de)lithiation of the working electrode. The first cycle coulombic efficiency (CE) is the ratio of the deliverable discharge and charge capacities for a battery; higher CE represents a more efficient SEI formation and lower irreversible capacity loss. For long-term testing, an accelerated C-rate is often used to increase the throughput of data collection; however, the RPT protocol is necessary when comparing the deliverable capacity of a

cell after cycling. Han *et al.* provide an example of battery cycling for state-of-health determination in LIBs for EVs using an RPT to compare the performance of batteries after an ageing/cycle life test (Figure 14).[114]

To test the rate capability of a coin-cell, a series of sequential charge and discharge steps was added with increasing C-rate. The deliverable capacity of the cell was then measured at each C-rate and compared as a fraction of the capacity of the cell from the RPT. Conventional rate capability tests use C-rates of C/10, C/5, C/2, 1C, 2C, and 5C (where 1C is the current required to charge or discharge the battery in 1h) while batteries with higher rate performance can be tested up to 10C and compared against the RPT which is cycled using a low rate of either C/20 or C/50.

For this thesis, the coin-cells were rested for 3-4h prior to electrochemical cycling in order to stabilize the battery after assembly. The initial capacity, CE, cycle life, and rate capability were measured and compared using various protocols, all of which will be highlighted in the following chapter.

3. Results and Discussion

This section will discuss the experimental decisions made to optimize the composition, synthesis parameters, electrode preparation and coating selection. The impact of each decision will be highlighted in the relevant physical and electrochemical characterization of the materials.

3.1 Optimizing Composition

The first step in the optimization process was to determine the initial material composition that would be used for the study. A detailed literature review revealed that numerous disordered rocksalt compositions have been reported to have high gravimetric capacity but suffer from low capacity retention, making them ideal candidates for optimization. $Li_{1.3}Nb_{0.3}V_{0.4}O_2$ (270mAh.g^{-1}),[65] $Li_2Mn_{2/3}Nb_{1/3}O_2F$ (320mAh.g^{-1}),[67] and $Li_{1.25}Mn_{0.5}Nb_{0.25}O_2$ (290mAh.g-1)[115] were initially considered as baseline materials; however, it became apparent that nickel has not been commonly used in reported materials which opened the design space for a composition to be developed and optimized from the ground up. The initial compositions that were synthesized for the baseline material used in this thesis were $Li_{1.25}Mn_{0.5}Nb_{0.25}O_2$ (LMNO), $Li_{1.3}Mn_{0.4}Nb_{0.3}O_2$ (LMNO-1.3), $Li_{1.3}Ni_{0.4}Nb_{0.3}O_2$ (LNNO), $Li_2Ni_{2/3}Nb_{1/3}O_2F$ (LNNOF). These materials were all prepared similarly as described in chapter 2. Precursors of Mn_2O_3, Nb_2O_5 and NiO were used at their respective compositions with Li_2CO_3 and LiOH used as lithium sources for LMNO, LMNO-1.3, and LNNO while Li_2CO_3 and LiF were used in LNNOF. The precursors were manually ground until homogenous in appearance and sintered at 950ºC for 12h under argon flow. The active material powders were prepared into electrodes using the E1 method described in section 2.4 and assembled into coin-cells.

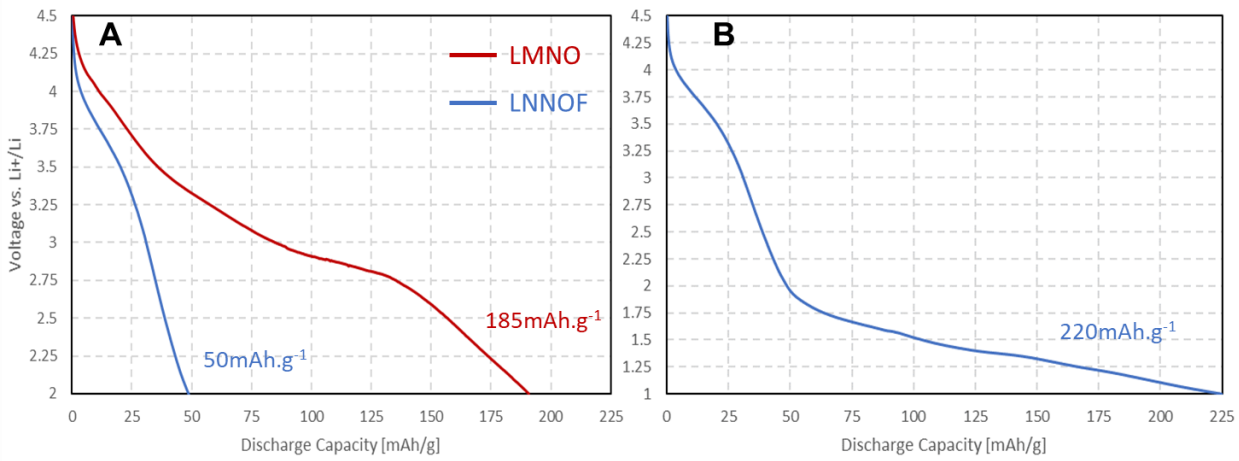

Figure 15 - First cycle charge and discharge voltage vs. capacity curve for $Li_{1.25}Mn_{0.5}Nb_{0.25}O_2$ (C/40, 25ºC), and $Li_2Ni_{2/3}Nb_{1/3}O_2F$ (C/40, 25ºC) between A) 2.0-4.5V vs. Li^+/Li; and B) 1.0-4.5V vs. Li^+/Li.

An RPT was run on each coin-cell over the voltage range of 2.0-4.8V vs. Li^+/Li (LMNO, LMNO-1.3) or 1.0-4.8V vs. Li^+/Li (LNNO, LNNOF) at C/40 rate and 25ºC. Analyzing the first cycle voltage vs. capacity curves for each material clearly indicated a potential issue with the Ni-based compositions. Figure 15 compares the first cycle for LMNO and LNNOF coin-cells. Despite reaching a higher discharge capacity of ~220mAh.g^{-1}, LNNOF gained only 22% of its deliverable capacity above 2.0V, shown in Figure 15A, compared to 100% of the 185mAh.g^{-1} that LMNO was capable of reaching above 2.0V. The low voltage plateau of the LNNOF material shown in Figure 15B was caused by the direct reduction of nickel within the structure. This low average voltage is a major inhibitor to potential commercialization of the material for next-generation EVs. For this thesis, the decision was made to move forward with the manganese-based LMNO and LMNO-1.3 compounds due to the higher average voltage. Specifically, the focus was on LMNO as no clear advantage in terms of electrochemical performance was observed in LMNO-1.3 samples and lower lithium and niobium content without losing performance is advantageous for a reduced battery cost and potential strain on the supply structure of those resources when used at the industrial scale.

A precursor material ($Mn_{0.66}Nb_{0.33}CO_3$) was then prepared by Hunan Zoomwe New Energy Science & Technology Co., LTD for the synthesis optimization of LMNO. Figure 16 shows the SEM images for $Mn_{0.66}Nb_{0.33}CO_3$. It was observed from Figure 16B that the primary particle morphology is polycrystalline separated by void space. The particle size distribution had some variance with average particles having a diameter of ~5-10µm. The large precursor particle size was ideal for the formation of a large single crystal final product; however, high temperature sintering would also cause the densification (removal of the void space) as the crystal grains grow together leading to a smaller particle size in the final product.

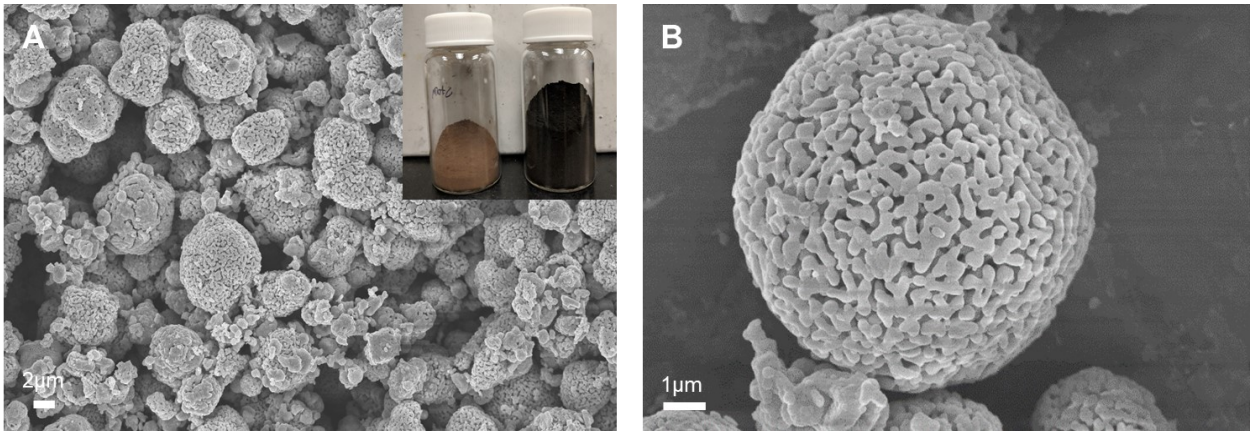

Figure 16 – SEM images of $Mn_{0.66}Nb_{0.33}CO_3$ precursor particles. A (inset) – left: $Mn_{0.66}Nb_{0.33}CO_3$ before pre-treatment, right: $Mn_{0.66}Nb_{0.33}CO_3$ after pre-treatment

3.2 Optimizing Synthesis

As the composition of the material had been determined, the focus shifted to optimization of the cycling stability and rate capability. As reported by Wang *et al.*, the capacity retention of polycrystalline $Li_{1.25}Mn_{0.5}Nb_{0.25}O_2$ without optimization is around 70-75% after 25 cycles at 25ºC leaving considerable room for improvement.[115] Furthermore, no long-term cycling data has been reported for this material. As noted in section 1.2.4, the high voltage cycling capability of DRX

cathodes can lead to accelerated loss of oxygen at the surface and surface reconstruction and nanovoid formation that can lead to structural collapse. Modification of the particle morphology to reduce the available surface area for oxygen loss to occur was a primary goal. This was accomplished through the synthesis of the active material with a single crystal morphology.

Numerous aspects of the synthesis procedure had to be adjusted in order to form a homogenous single crystal material with acceptable performance including sintering temperature, dwell time and use of a salt flux. LMNO with polycrystalline morphology was synthesized in accordance with the work of Wang *et al*. by dry ball milling oxide precursors with a lithium source at 300rpm for 5h. The homogenous powder was then sintered at 950ºC for 12h under nitrogen gas flow. To synthesize LMNO with a single crystal morphology the addition of excess lithium and a non-oxidizing salt to the precursor powder provided a flux-like environment to facilitate particle growth.[116] For single crystal LMNO a large batch was prepared from either oxide or carbonate precursors and dry ball milled at 300rpm for 5h. An additional 10 mol% Li_2CO_3 was added before sintering to compensate for evaporation of lithium during sintering. KCl was also added and manually ground until well mixed. The powder was then sintered at 950ºC for 12-36h under nitrogen gas flow.

SEM was used confirm the different morphologies of the synthesized materials. The multi-faceted appearance of the particles in Figure 17A are indicative of a polycrystalline structure. In contrast, the large, smooth particles in Figure 17B,C suggest that during synthesis, the crystal facets had a similar thermodynamic stability causing growth at the same rate and the formation of a large single crystal absent of grain boundaries.

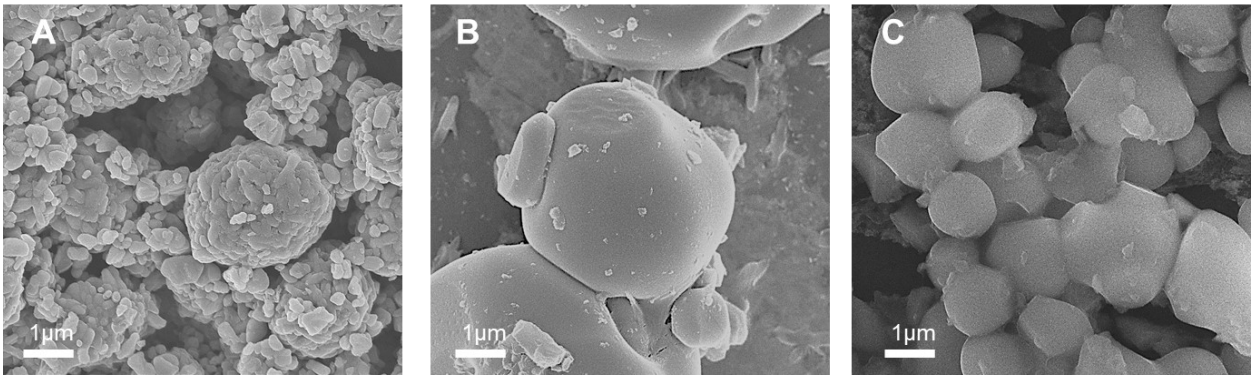

Figure 17 - SEM images of A) Polycrystalline LMNO; B) Single Crystal LMNO ($Mn_{0.66}Nb_{0.33}CO_3$.); and C) Single crystal LMNO (Li_2CO_3, Mn_2O_3, and Nb_2O_5)

To confirm that the correct material had been synthesized, XRD was performed on the single crystal LMNO (Figure 18). Refinement was carried out on the 2Θ range of 5-90° using the Fm-3m space group for $LiFeO_2$. It is assumed that the rocksalt structure contains a random arrangement of Li, Mn and Nb in the 4b position (½, ½, ½) with the O atom fixed in the 4a position (0, 0, 0). Using this model, the refinement yielded a lattice spacing of (a) = 4.1940Å which is relatively close to the reported spacing for $Li_{1.25}Mn_{0.5}Nb_{0.25}O_2$ at (a) = 4.1738Å. Major peaks at 2Θ = 36°,43°, 62°, 75°, and 79° all correspond to those reported in literature for this composition indicating low impurity content.

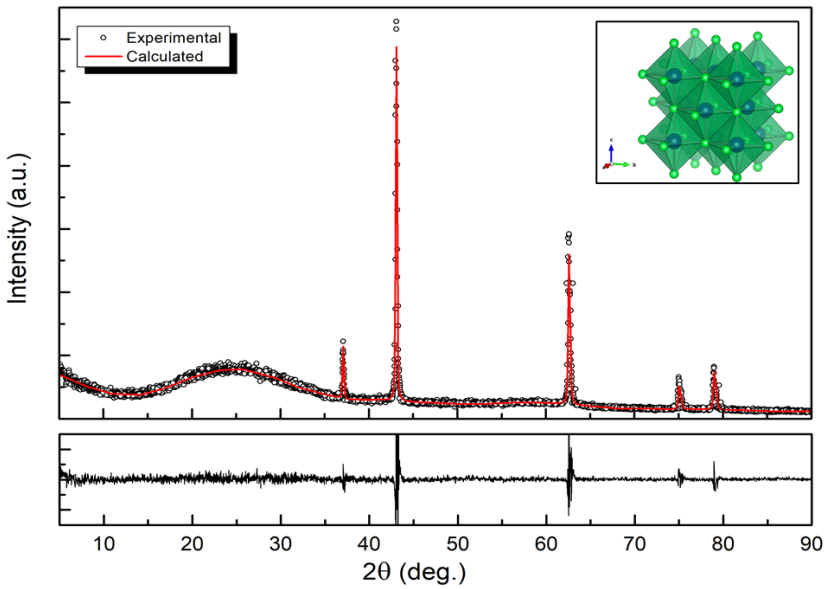

Figure 18 - XRD pattern for single crystal LMNO (Li_2CO_3, Mn_2O_3, and Nb_2O_5); inset: ball-stick model of disordered rock-salt structure (blue: Mn, Nb, Li; light-green: O)

Optimization of the synthesis process involved the systematic investigation of each factor on the morphology and performance of the cathodes. Table 1 summarizes the sintering procedures, excess lithium content, and type of precursor material used in the synthesis process. The table is organized based on chronological order, with the earliest prepared materials at the top and those synthesized most recently at the bottom.

The optimization included the use of surface coatings as described in section 2. After a material was prepared, preliminary physical and electrochemical testing was done to confirm the morphology and initial performance of the material was inline with the goals of the experiment. The coating process was then done on these materials, indicated in Table 1 as a precursor. Figure 20 shows a performance comparison of these materials, and the effects of varying the synthesis conditions are discussed below.

Table 1 - Summary of synthesis methods used to prepare $Li_{1.25}Mn_{0.5}Nb_{0.25}O_2$

ID #	Excess Li	Sintering Procedure	Coating	Precursor
OS-001	5%	500°C 3h, 800°C 3h, 950°C 24h	1wt% PAN	Li_2CO_3, $Mn_{0.66}Nb_{0.33}CO_3$ (850°C 6h)
OS-002	0%	950°C 24h	–	Li_2CO_3, $Mn_{0.66}Nb_{0.33}CO_3$ (850°C 6h)
OS-003	0%	950°C 24h	1wt% PAN	OS-002
SH-001	5%	950°C 12h (x2) - Ar flow	1wt% PAN	SH-002
SH-002	5%	950°C 12h (x2) - Ar flow	–	Li_2CO_3, $Mn_{0.66}Nb_{0.33}CO_3$ (850°C 6h)
SH-003	3%	950°C 12h (x2) - Ar flow	–	Li_2CO_3, $Mn_{0.66}Nb_{0.33}CO_3$ (850°C 6h)
SH-004	5%	950°C 12h (x3) - N_2 flow	–	SH-002
SH-005	5%	950°C 12h (x3) - N_2 flow	1wt% PAN	SH-004
SH-006	5%	850°C 6h, 950°C 12h, 950°C 24h - N_2 flow	–	Li_2CO_3, $Mn_{0.66}Nb_{0.33}CO_3$ (850°C 6h)
SH-007	5%	850°C 6h, 950°C 12h, 950°C 24h - N_2 flow	1wt% PAN	SH-006
SH-008	5%	500°C 6h - N_2 flow	2wt% LBCO	SH-004
SH-009	15%	950°C 36h - N_2 flow (2.5h ramp)	–	Li_2CO_3, $Mn_{0.66}Nb_{0.33}CO_3$ (600°C 3h)
SH-010	10%	950°C 12h - N_2 flow (2.5h ramp)	–	Li_2CO_3, $Mn_{0.66}Nb_{0.33}CO_3$
SH-011	10%	950°C 36h - N_2 flow (2.5h ramp)	–	Li_2CO_3, $Mn_{0.66}Nb_{0.33}CO_3$
SH-012	0%	950°C 6h - N_2 flow (2.5h ramp)	–	Li_2CO_3, $Mn_{0.66}Nb_{0.33}CO_3$
SH-013	0%	950°C 12h - N_2 flow (2.5h ramp)	–	Li_2CO_3, $Mn_{0.66}Nb_{0.33}CO_3$
SH-014	0%	950°C 36h - N_2 flow (2.5h ramp)	–	Li_2CO_3, $Mn_{0.66}Nb_{0.33}CO_3$
SH-015	0%	950°C 6h – N_2 flow (2.5h ramp)	–	Li_2CO_3, Nb_2O_5, Mn_2O_3

SH-016	10%	950°C 12h – N_2 flow (2.5h ramp)	–	Li_2CO_3, $Mn_{0.66}Nb_{0.33}CO_3$
SH-011_ALD	–	–	5 Cycle ALD of Al_2O_3	SH-011
OS-E13	5%	Ball mill 5h, 950°C 12h - Ar flow (3.5h ramp)	–	Li_2CO_3, Nb_2O_5, Mn_2O_3
SH-011B	10%	950°C 24h - N_2 flow (2.5h ramp)	–	Precursor (600'C 3h)
SH-011B_ALD	–	–	5 Cycle ALD of Al_2O_3	SH-011B
SH-017	5%	850°C 6h, 950'C 12h, 950'C 24h - N_2 flow	–	Precursor (850'C 6h)
SH-017_LBCO	–	600°C 10h - Ar flow	2wt% LBCO	SH-017, Li_2CO_3, LiOH, H_3BO_3
SH-018	10%	950°C 12h - N_2/Ar flow (2h ramp)	–	Li_2CO_3, Nb_2O_5, Mn_2O_3
SH-018_LBCO	–	600°C 10h - Ar flow	2wt% LBCO	SH-018, Li_2CO_3, LiOH, H_3BO_3
SH-018_ALD	–	–	5 Cycle ALD of Al_2O_3	SH-018
SH-018_PAN	–	450°C 2h ramp, 30min hold - N_2/Ar flow	1wt% PAN	SH-018

3.3 Optimizing Electrochemical Cell Preparation

The performance of lithium-ion batteries is not solely determined by the active material powder, and when optimizing cathode materials, it is critical to consider the impact of all components. Since the electrode composition has been reported to have an affect on the conductivity and stability of the battery, numerous groups have investigated the inclusion of various binders and conductive additives to improve the performance or commercialization potential of novel lithium-ion batteries.[91,117] E1 was initially used for electrode preparation due to the widespread use of the method for commercial production of LIB electrodes. The method is capable of high throughput, with 1g of active material capable of producing >30 individual electrodes in 1-2h. However, due to the 90:5:5 active material:binder:conductive additive ratio,

problems with the consistency of mixing or coating homogeneity between batches are likely, leading to poor repeatability of performance. To solve this problem E2 was used to increase the accuracy in batch-to-batch active material mass; however, the throughput of this method was drastically reduced from E1 to ~1 electrode prepared in 1-2h.

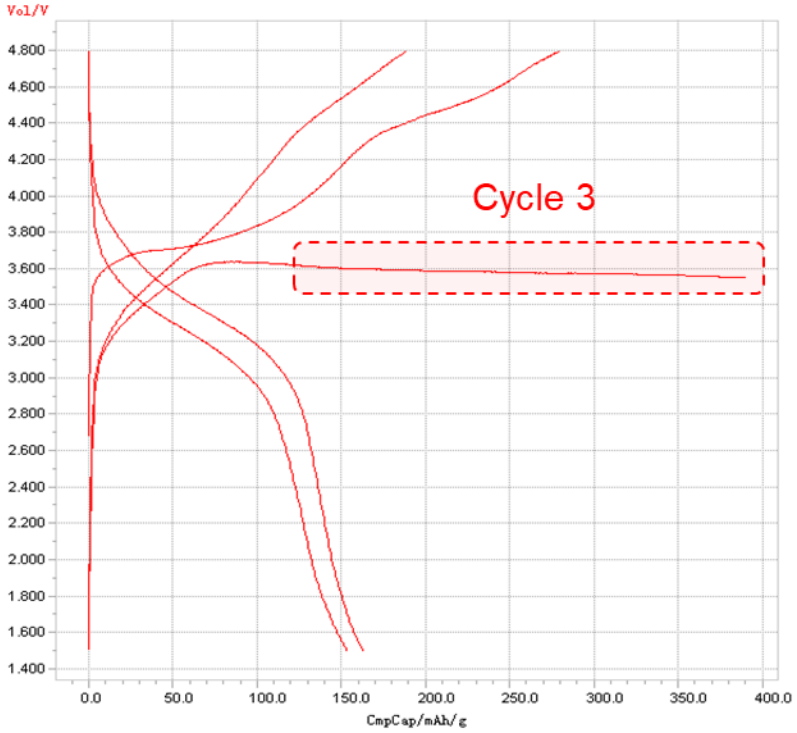

Figure 19 - Poor cycle performance caused by high moisture content in the electrode

Another difficulty with the E2 preparation method was the absorption of moisture into the electrodes. Water content in the cells is a major problem as it can undergo parasitic side reactions with the lithium salt ($LiPF_6$) leading to the formation of gaseous hydrogen fluoride and decomposition of the electrolyte (Eqn 3.1).[118,119]

$$LiPF_6 + H_2O \rightarrow 2HF + LiF + POF_3 \quad (3.1)$$

The decreasing voltage occurring during the 3rd charge cycle shown in Figure 19 for an electrode prepared using the E2 method was associated with this reaction. Cells that incurred this issue eventually resumed charging after >100h, once all moisture had been removed from the electrode by complete conversion to the products listed in Eqn 3.1. The performance was degraded on subsequent cycles. Electrodes were then prepared using method E3 based on the work of Park *et al*. which increased production throughput to similar levels as E1, with over 20 punched electrodes prepared within 1 hour, but allowed for high precision of active material mass due to the high fraction of active material powder relative to additives.

3.4 Electrochemical performance

Throughout the optimization process, electrochemical testing was performed to measure the viability of the material as a LIB cathode. The initial charge and discharge performance of the material along with the 5-cycle capacity retention at C/20 rate were measured for all materials, further electrochemical characterization (*i.e.* cycling retention, rate capability, *etc.*) was carried out for selected samples. A summary of the initial electrochemical results for 1st cycle reversible capacity, CE, and 5-cycle capacity retention for all materials specified in Table 1 is displayed in Figure 20. The “acceptable” and “ideal” highlighted sections in Figure 20 represent a qualitative measurement of how the material performed relative to others displayed. A higher 1st cycle discharge capacity (>200mAh.g-1) and fractional capacity (~1.00) are key metrics of battery performance. The classification of these materials relative to others prepared with a different methodology assisted in the optimization process by providing insight to which factors lead to better performance

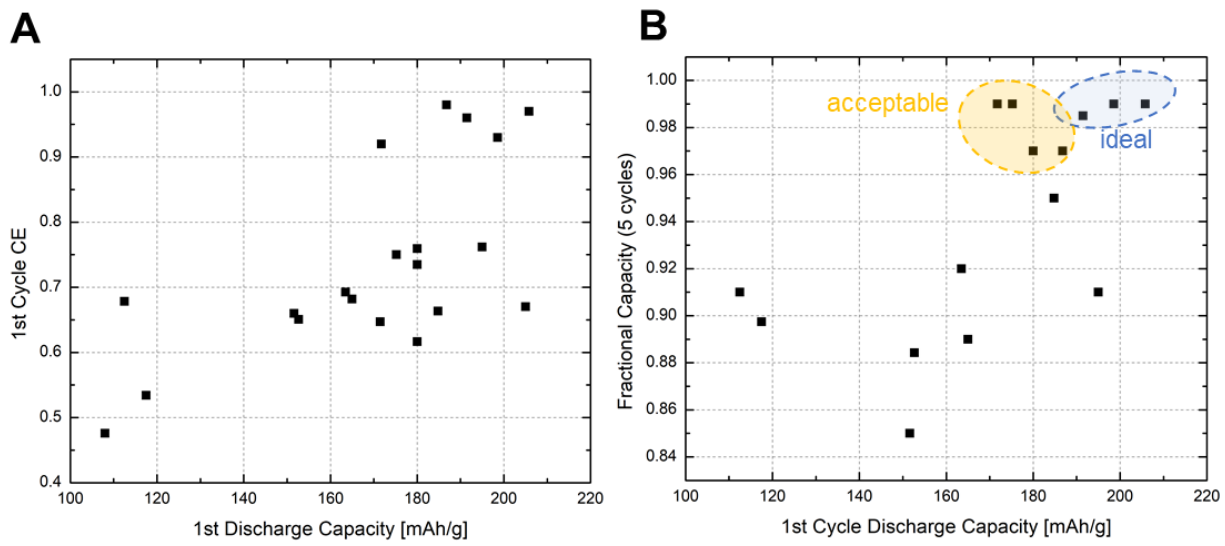

Figure 20 - Summary of electrochemical performance for all materials prepared during optimization process. A: 1st cycle discharge capacity vs. coulombic efficiency; B: 1st cycle discharge capacity vs. fractional capacity retention after 5 cycles (C/20).

It was found that sintering time had an impact on the 1st cycle discharge capacity, as SH-002 (950ºC for 24h) delivered only 160mAh.g^{-1} compared to the 180mAh.g^{-1} of SH-004 (950ºC for 36h). The CE was not affected by adjusting the sintering time with both samples reaching ~70%. Lithium content was also found to have an impact on the performance of the material. Samples SH-011 and SH-014 were both sintered at 950ºC for 24h with all parameters other than initial lithium content kept the same. Sample SH-011 had +10 mol% excess Li_2CO_3 added during the pre-treatment phase and delivered 184mAh.g^{-1} after the 1st cycle discharge at C/20 rate between 2.0-4.8V vs. Li^+/Li. In comparison, sample SH-014 delivered only 171mAh.g^{-1} after the 1st cycle discharge with the same conditions. During heat-treatment, lithium added to the precursor can be lost by evaporation as Li_2O preventing the complete lithiation of the positive electrode material. DRX materials enable lithium enrichment in the lattice allowing them to reach high capacities; however, if too much lithium is lost during the heat-treatment step, the capacity of the material will decrease. It was found that +10 mol% was sufficient to compensate for lithium loss at 36h as

SH-009 was prepared using +15 mol% Li_2CO_3 with all other synthesis conditions kept the same as SH-011 and a similar 1st cycle discharge capacity of 180mAh.g^{-1} was delivered. Optimization of battery performance required constant iteration during synthesis. Adjustments made to dwell time during sintering and initial lithium content were found to have the greatest effect on initial discharge capacity with a longer dwell time (36h) and +10 mol% excess lithium proving to be critical parameters in preparing a positive electrode material capable of delivering >180mAh.g^{-1}.

3.4.1 First cycle capacity

The first cycle discharge curves for uncoated polycrystalline (SH-015), uncoated single crystal (SH-016), 1wt% LBCO coated single crystal (SH-018_LBCO), and Al_2O_3 coated single crystal (SH-018_ALD) samples are compared in Figure 21. The coin-cells were cycled within the voltage window of 2.0-4.8 V vs. Li^+/Li at a constant rate of C/20 at 40ºC. SH-018_LBCO delivered the highest capacity (189mAh.g^{-1}) of the compared samples, similar to the polycrystalline SH-015 (185mAh.g^{-1}). The uncoated single crystal SH-016 sample delivered the lowest capacity (165mAh.g^{-1}), due to the larger grain size causing slightly more sluggish lithium diffusion kinetics. The impact of both applied surface coatings is indicated by the increased average voltage of the material. Uncoated single and polycrystalline samples delivered only 45% and 48% of their total discharge capacity above 3.0V respectively, while both SH-018_ALD and SH-018_LBCO delivered 94% and 92% respectively. The flat voltage plateau and sharp turn in the coated samples is indicative of a lower impedance of the system owing to the improved conductivity of the coatings. Specifically, the LBCO type coating showed the greatest improvement over the uncoated materials allowing single crystal LMNO to reach the same capacity as the polycrystalline LMNO material.

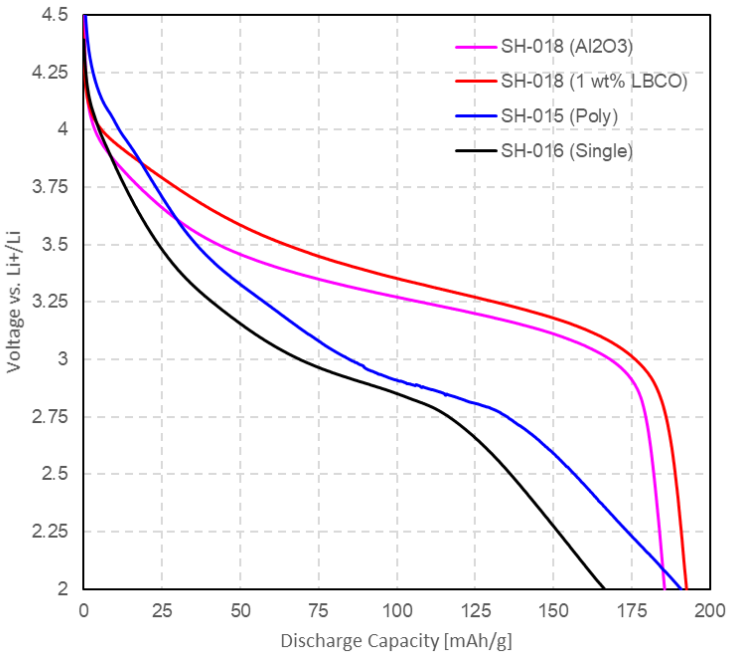

Figure 21 - 1st cycle discharge curves (2.0-4.8 V vs. Li^+/Li, C/20, 40°C) for uncoated polycrystalline, uncoated single crystal, single crystal with Al_2O_3 coating, single crystal with LBCO coating

3.4.2 Capacity retention

Uncoated single and polycrystalline LMNO samples were cycled within the voltage window of 2.0-4.8V vs Li^+/Li for 40 cycles at 40°C. Figure 22 shows the comparison of the cycling discharge profiles of the two different morphologies of LMNO. Polycrystalline LMNO retained only 50% initial capacity after 40 cycles while the single crystal sample retained 80%. The rapid capacity loss of the polycrystalline material is consistent with reported literature and is attributed to the increased oxygen loss and active material dissolution in the cathode due to a greater exposed surface for reaction with the electrolyte. The results show a clear improvement in the cyclability of the single crystal material with the trade-off of a slightly lower initial capacity.

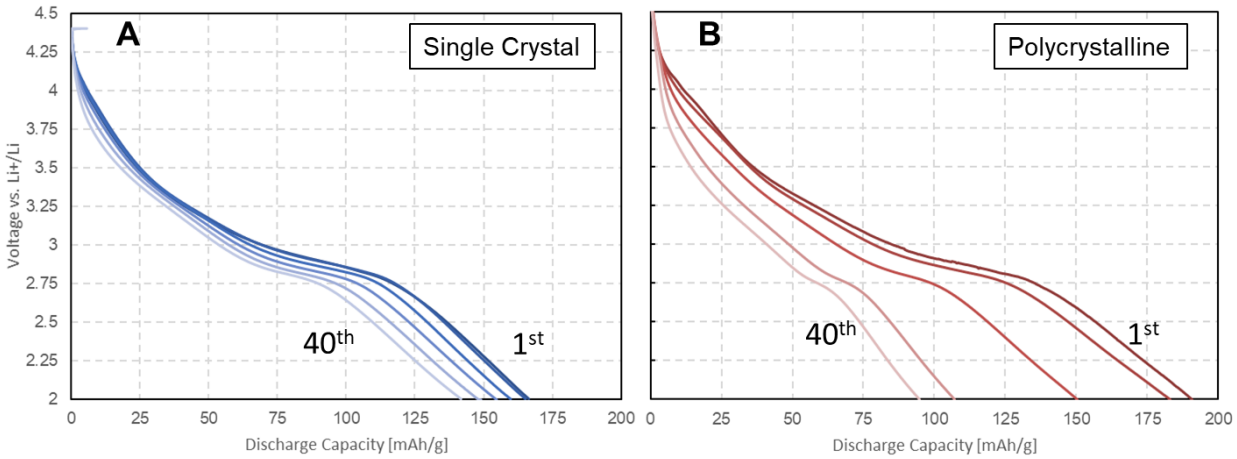

Figure 22 - Long term cyclability of A: uncoated single crystal LMNO (SH-016); and B: uncoated polycrystalline LMNO (SH-015). Discharge curves for 1st, 10th, 20th, 30th, and 40th cycles.

The cycling performance of coated and uncoated LMNO was compared alongside the different particle morphologies in Figure 23. The rapid capacity fade observed in the uncoated polycrystalline (SH-015) material previously is confirmed by the "knee" in deliverable capacity after 15 cycles. The single crystal material prepared from the $Mn_{0.66}Nb_{0.33}CO_3$ precursor (SH-016) retained 86% initial capacity after 25 cycles, an improvement over the 76% delivered by SH-015. Furthermore, the uncoated single crystal material prepared from Li_2CO_3, Nb_2O_5, Mn_2O_3 precursors (SH-018) had cyclability of 98% retention after 25 cycles and 88% retention after 50 cycles. SH-018 was coated with a nanometer thick film of Al_2O_3 (SH-018_ALD) performed worse than the uncoated material over the first 15 cycles delivering 95% initial capacity. As this does not indicate a substantial benefit as speculated, it is proposed that long-term cycling could be done to investigate the benefit of the Al_2O_3 coating after 50-100 cycles. SH-018 coated with 1wt% PAN (SH-018_PAN) as described in section 2 performed equally to the Al_2O_3 coating with a retention of 95% after the first 15 cycles. Unlike the Al_2O_3 and PAN surface treatments, SH-018 coated with 1wt% LBCO was only tested for 7 charge and discharge cycles due to time constraints, delivering an initial capacity of 205mAh.g^{-1} with a 99% capacity retention. It is clear that further testing is

needed to completely characterize the impact that each coating has on the long-term cycling performance of the LMNO material; however, improvement has been shown in the initial cycling results for the LBCO coating and in the initial discharge capacity for both Al_2O_3 and PAN coatings over the uncoated single crystal LMNO.

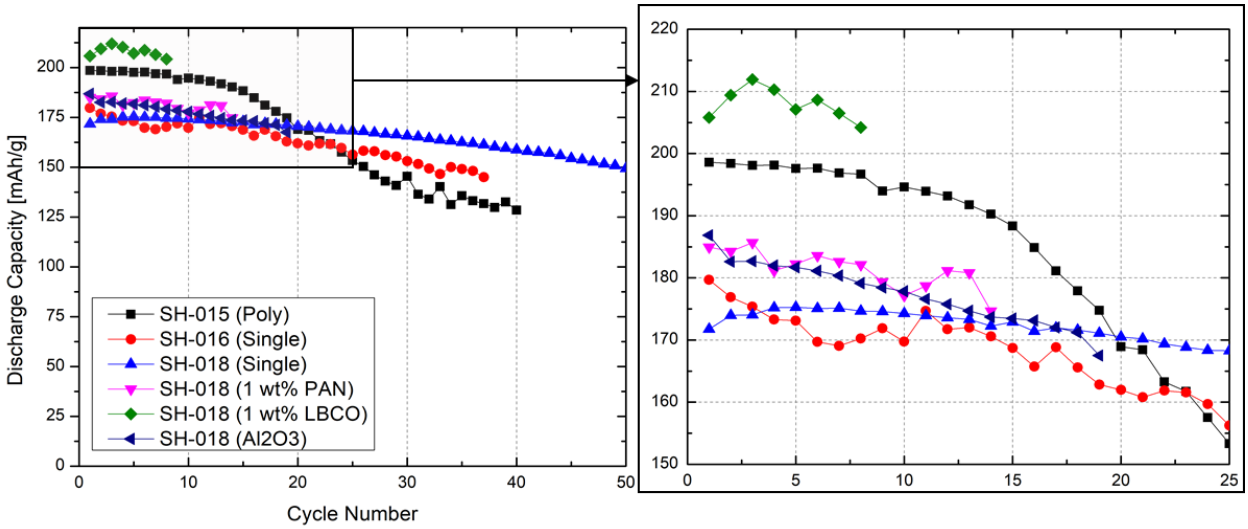

Figure 23 - Cycling stability comparison for LMNO with polycrystalline or single crystal morphology and various surface modifications.

3.4.3 Rate capability

The effects of the LBCO coating on the performance of the LMNO material at elevated discharge rates are illustrated in Figure 24. The current rate was increased from C/20 to C/10, C/5, and C/2 showing slight separation between uncoated SH-018 and LBCO coated SH-018. However, the rate performance of the coated material did not show any significant benefit. This result indicated that the rate capability of LMNO was still limited by the sluggish lithium diffusion pathways intrinsic to DRX materials and reduction of interfacial resistance was not the factor bottlenecking the high rate performance.

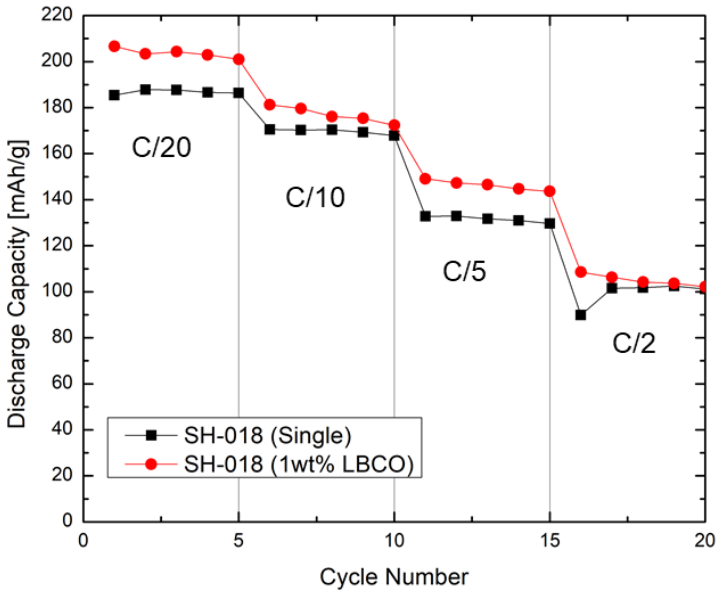

Figure 24 - Rate capability comparison between uncoated and 1wt% LBCO coated single crystal LMNO

4. Future Work

Despite the ambitious scope of this project and some of the improvements described, future work is still needed to produce a DRX material with high commercialization potential. Furthermore, numerous challenges were encountered throughout the course of this project that caused delays to the experimental aspects of the study limiting data collection and sample preparation. These challenges will be highlighted in the limitations of study. This section examines potential shortcomings in the work presented within this thesis and provides insight to the future directions that could complete the larger scope of the project.

4.1 Long-term cycling

Preliminary cycling results for several samples have been discussed in section 3, providing a basic understanding of the effects of particle morphology and surface treatment on the electrochemical stability of the material. This, however, is a shortcoming of many reports investigating DRX materials, as the low rate capability of the material typically only allows for charge and discharge operation at low current (*i.e.* C/100, C/50) therefore limiting the speed of data collection and inhibiting the use of these materials for commercial application. Furthermore, the effects of each coating and particle morphology may become more pronounced as the cell is aged due to reduced impedance growth, or mitigation of a structural degradation pathway such as oxygen loss. The greatest limitation for this is the time it takes for collection of cycling data due to the low rate requirement. An area of potential continuation for this project is the analysis of long-term cycling (>100 cycles) data for each sample. The repeatability of this cycling performance should also be investigated, as even slight changes to the cell assembly or electrode preparation could impact the performance of the sample. This could be done through the parallel

testing of 3-5 coin-cells for each sample. A strategy to reduce the data collection time would be the continued development of a fast charge voltage profile, using a combination of constant current-to-voltage (CCV) and constant voltage-to-current (CV) charging protocols as shown in Figure 24, in what is referred to as a "step charge" profile. Increasing the initial current to C/10, C/5 during CCV charging, then followed by a brief rest allowing for the voltage to drop slightly before another CCV charging step at C/20. The cell could be rested an additional time and a CV charge to hold the cell at the upper cut off voltage could be run to ensure complete delithiation of the cathode. This step charge profile could be repeated on discharge and would allow for a faster rate of data collection without sacrificing the deliverable capacity of the material.

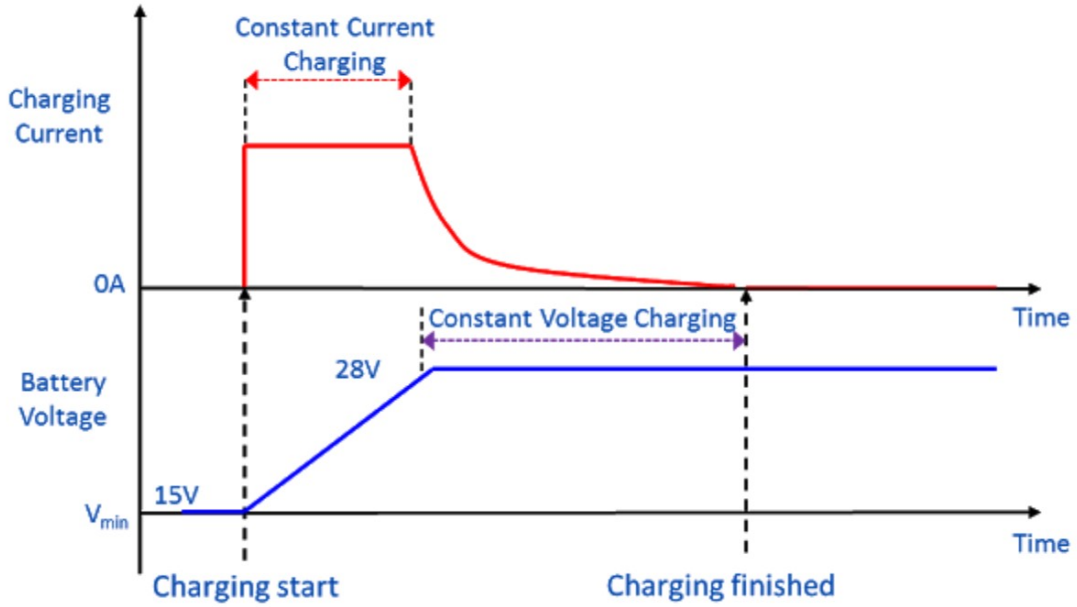

Figure 25 - Diagram of constant current-to-voltage (CCV) and constant voltage-to-current (CV) charging [120]

4.2 Thermal stability

The thermal stability of the DRX material was not investigated within this thesis; however, several methods for the complete characterization of the safety and stability of a LIB cathode

material at high temperature were outlined in section 2. This is a necessary characterization step if the material is to be considered for its commercialization potential, specifically, comparative analysis of ARC data for coated and uncoated LMNO samples vs those reported in literature.

4.3 Coating characterization

Physical characterization of the Al_2O_3, LBCO, and PAN coatings is another area of future work. Optimization of the sample performance could be improved by testing the effects of different coating thicknesses, which could be characterized through transmission electron microscopy (TEM). Furthermore, elemental analysis of the coated sample to show the coating distribution and check for homogeneity could be done through EDX as mentioned in section 2.7.

4.4 Ex-situ characterization

The differences in degradation mechanisms for the polycrystalline and single crystal DRX materials could be further investigated through ex-situ physical characterization. This thesis reports the results of a preliminary cycling test with single crystal morphology showing improvement in capacity retention over the polycrystalline sample. The mechanistic explanation for these results could be examined in more detail by disassembling the cells after cycling and studying the cycled electrodes with XRD and SEM. This could provide insight to the potential phase transitions of morphological changes occurring within the cathode material during cycling.

4.5 Limitations of Study

Due to the shutdown of the University of Waterloo in the Spring 2020 term, several characterization methods were unable to be completed for the synthesized material. This includes

but was not limited to the thermogravimetric analysis (TGA) and accelerating rate calorimetry (ARC) used to determine thermal stability of the cathode, electrochemical impedance spectroscopy (EIS) to measure the bulk, charge transfer, and mass transfer resistance, and systematic long-term cycling (>100 cycles) for all materials. The results obtained prior to the shutdown were presented within the body of this thesis and detailed.

5. Conclusions and Perspectives

$Li_{1.25}Mn_{0.5}Nb_{0.25}O_2$ (LMNO) particles with a single crystal morphology were synthesized with low impurity content through high temperature, flux-mediated sintering. The particle morphology was modified by systematically adjusting synthesis parameters including sintering temperature, dwell time, lithium excess content, and precursor composition as discussed in section 2. Synthesis of single crystal particles with good electrochemical performance was optimized to have a sintering temperature of 950°C, 12h dwell time, and +10 mol% excess lithium (Li_2CO_3) added to the precursor oxides. The composition of the material was identified through XRD and the particle morphology was confirmed using SEM. The materials were prepared into electrodes and assembled into coin-cell half-cells that were then characterized through battery cycling at various current rates and voltage windows.

Single crystal LMNO delivered initial discharge capacity of 165mAh.g^{-1}, slightly lower than the capacity delivered by polycrystalline LMNO sample of 185mAh.g-1. This decrease in capacity was attributed to the larger single crystal particles increasing the diffusion length of lithium ions in the crystal, an already sluggish process for DRX cathodes. However, the single crystal sample displayed considerably better cycling retention than the polycrystalline material at 80% of 165mAh.g^{-1} and 50% of 185mAh.g^{-1} respectively after 40 cycles over the voltage range of 2.0-4.8V vs Li^+/Li at C/20 rate and at 40°C. The single crystal LMNO was coated with several different materials including conductive $2Li_2O$-B_2O_3 (LBCO), and polyacrylonitrile (PAN) through solvent casting and ALD of Al_2O_3 for 10 cycles. The purpose of the coatings was to assist with the adjusted morphology in stabilizing the particle surface by protecting it from parasitic reactions with the electrolyte and acting as a physical barrier to inhibit surface level oxygen loss. The ALD- and

PAN-coated single crystal LMNO delivered similar initial discharge capacity ~185mAh.g^{-1}, a considerable improvement over the uncoated material; however, the LBCO coating performed the best with a 189mAh.g^{-1} discharge capacity. The initial cycling retention of these materials was investigated showing no notable improvement over the uncoated samples after 15 cycles. It is recommended that long-term cycling (>100 cycles) be performed on both coated and uncoated single crystal samples to expand upon the work done within this thesis. It would be an appropriate extension of this thesis to expand the range of coatings tested, as the use of Al_2O_3 and LBCO coatings for single crystal DRX cathodes showed substantial improvement to the average voltage during discharge. For example, the conductive polymer coating (poly(3,4-ethylenedioxythiophene)) (PEDOT) recently examined by Xu *et al*. offers a range of benefits to battery performance including the mitigation of oxygen loss and conductivity to lithium ions and electrons.[121] The rate capability was also investigated, with no significant benefit observed between the LBCO and uncoated single crystal LMNO. This suggested that the underlying problem with rate performance in DRX materials was the sluggish lithium diffusion kinetics. Surface modification to reduce interfacial resistance was not an effective strategy to improve the rate capability.

DRX materials remain a promising new class of cathodes for LIBs with high theoretical energy density, high safety metrics, and without a reliance on potentially unsustainable resources such as cobalt. However, despite these characteristics, significant challenges must be overcome before this material is ready for commercialization, specifically their low stability and rate performance. Although this thesis showed improvements to the cycling retention for the DRX LMNO material with a single crystal morphology, the long-term effects of this modification were not completely

investigated. Furthermore, no improvements to the rate capability of the material were made through the application of the selected surface coatings. Taken together it is necessary for additional research to be done in order to push DRX cathodes into commercialization for next-generation LIBs

References

1. Cano, Z.P., Banham, D., Ye, S., Hintennach, A., Lu, J., Fowler, M., and Chen, Z. (2018). Batteries and fuel cells for emerging electric vehicle markets. Nat. Energy *3*, 279–289.
2. Energy Technology Perspectives 2017 – Analysis - IEA https://www.iea.org/reports/energy-technology-perspectives-2017.
3. World economic forum (2019). A Vision for a Sustainable Battery Value Chain in 2030 Unlocking the Full Potential to Power Sustainable Development and Climate Change Mitigation.
4. Andre, D., Kim, S.J., Lamp, P., Lux, S.F., Maglia, F., Paschos, O., and Stiaszny, B. (2015). Future generations of cathode materials: An automotive industry perspective. J. Mater. Chem. A *3*, 6709–6732.
5. DOE Annual Merit Review (2012).
6. Kobayashi, Y., Tabuchi, M., Miyashiro, H., and Kuriyama, N. (2017). A new design of highly reversible LiNiO 2 : Defect formation in transition metal site. J. Power Sources *364*, 156–162.
7. Noh, H.J., Youn, S., Yoon, C.S., and Sun, Y.K. (2013). Comparison of the structural and electrochemical properties of layered Li[NixCoyMnz]O2 (x = 1/3, 0.5, 0.6, 0.7, 0.8 and 0.85) cathode material for lithium-ion batteries. J. Power Sources *233*, 121–130.
8. Li, H., Li, J., Ma, X., and Dahn, J.R. (2018). Synthesis of single crystal LiNi0.6Mn0.2Co0.2O2 with enhanced electrochemical performance for lithium ion batteries. J. Electrochem. Soc. *165*, A1038–A1045.
9. Li, H., Li, J., Zaker, N., Zhang, N., Botton, G.A., and Dahn, J.R. (2019). Synthesis of Single Crystal LiNi 0.88 Co 0.09 Al 0.03 O 2 with a Two-Step Lithiation Method . J. Electrochem. Soc. *166*, A1956–A1963.
10. Berckmans, G., Messagie, M., Smekens, J., Omar, N., Vanhaverbeke, L., and Mierlo, J. Van (2017). Cost projection of state of the art lithium-ion batteries for electric vehicles up to 2030. Energies *10*.
11. Banza Lubaba Nkulu, C., Casas, L., Haufroid, V., De Putter, T., Saenen, N.D., Kayembe-Kitenge, T., Musa Obadia, P., Kyanika Wa Mukoma, D., Lunda Ilunga, J.M., Nawrot, T.S., et al. (2018). Sustainability of artisanal mining of cobalt in DR Congo. Nat. Sustain.

1, 495–504.

12. Battery megafactory capacity in the pipeline exceeds 2 TWh as solid state makes first appearance | Benchmark Mineral Intelligence https://www.benchmarkminerals.com/benchmarks-megafactory-tracker-exceeds-2-terawatt-hours-as-solid-state-makes-its-first-appearance/.
13. Petrucci, R.H.; Harwood, W.S. and Herring, F.. (2002). General Chemistry: Principles and Modern Applications 8th ed. (Prentice Hall).
14. Whittingham, M.S. (2004). Lithium batteries and cathode materials. Chem. Rev. *104*, 4271–4301.
15. Li, H., Wang, Z., Chen, L., and Huang, X. (2009). Research on advanced materials for Li-ion batteries. Adv. Mater. *21*, 4593–4607.
16. Manthiram, A. (2011). Materials challenges and opportunities of lithium ion batteries. J. Phys. Chem. Lett. *2*, 176–184.
17. Haregewoin, A.M., Wotango, A.S., and Hwang, B.J. (2016). Electrolyte additives for lithium ion battery electrodes: Progress and perspectives. Energy Environ. Sci. *9*, 1955–1988.
18. Gao, Z., Sun, H., Fu, L., Ye, F., Zhang, Y., Luo, W., and Huang, Y. (2018). Promises, Challenges, and Recent Progress of Inorganic Solid-State Electrolytes for All-Solid-State Lithium Batteries. Adv. Mater. *30*, 1–27.
19. Manthiram, A., Yu, X., and Wang, S. (2017). Lithium battery chemistries enabled by solid-state electrolytes. Nat. Rev. Mater. *2*, 1–16.
20. Lee, W., Muhammad, S., Sergey, C., Lee, H., Yoon, J., Kang, Y.M., and Yoon, W.S. (2020). Advances in the Cathode Materials for Lithium Rechargeable Batteries. Angew. Chemie - Int. Ed. *59*, 2578–2605.
21. Myung, S.T., Maglia, F., Park, K.J., Yoon, C.S., Lamp, P., Kim, S.J., and Sun, Y.K. (2017). Nickel-Rich Layered Cathode Materials for Automotive Lithium-Ion Batteries: Achievements and Perspectives. ACS Energy Lett. *2*, 196–223.
22. Julien, C., Mauger, A., Zaghib, K., and Groult, H. (2014). Comparative Issues of Cathode Materials for Li-Ion Batteries. Inorganics *2*, 132–154.
23. Nitta, N., Wu, F., Lee, J.T., and Yushin, G. (2015). Li-ion battery materials: Present and future. Mater. Today *18*, 252–264.

24. Buchberger, I., Seidlmayer, S., Pokharel, A., Piana, M., Hattendorff, J., Kudejova, P., Gilles, R., and Gasteiger, H.A. (2015). Aging Analysis of Graphite/LiNi 1/3 Mn 1/3 Co 1/3 O 2 Cells Using XRD, PGAA, and AC Impedance . J. Electrochem. Soc. *162*, A2737–A2746.
25. Qiu, C., He, G., Shi, W., Zou, M., and Liu, C. (2019). The polarization characteristics of lithium-ion batteries under cyclic charge and discharge. J. Solid State Electrochem. *23*, 1887–1902.
26. Xiao, Y., Liu, T., Liu, J., He, L., Chen, J., Zhang, J., Luo, P., Lu, H., Wang, R., Zhu, W., et al. (2018). Insight into the origin of lithium/nickel ions exchange in layered Li(NixMnyCoz)O2 cathode materials. Nano Energy *49*, 77–85.
27. Makimura, Y., Zheng, S., Ikuhara, Y., and Ukyo, Y. (2012). Microstructural Observation of LiNi 0.8 Co 0.15 Al 0.05 O 2 after Charge and Discharge by Scanning Transmission Electron Microscopy . J. Electrochem. Soc. *159*, A1070–A1073.
28. Zheng, S., Huang, R., Makimura, Y., Ukyo, Y., Fisher, C.A.J., Hirayama, T., and Ikuhara, Y. (2011). Microstructural Changes in LiNi0.8Co0.15Al0.05O2 Positive Electrode Material during the First Cycle. J. Electrochem. Soc. *158*, A357.
29. Abraham, D.P., Twesten, R.D., Balasubramanian, M., Kropf, J., Fischer, D., McBreen, J., Petrov, I., and Amine, K. (2003). Microscopy and Spectroscopy of Lithium Nickel Oxide-Based Particles Used in High Power Lithium-Ion Cells. J. Electrochem. Soc. *150*, A1450.
30. Watanabe, S., Kinoshita, M., Hosokawa, T., Morigaki, K., and Nakura, K. (2014). Capacity fade of LiAlyNi1-x-yCoxO 2 cathode for lithium-ion batteries during accelerated calendar and cycle life tests (surface analysis of LiAlyNi1-x-yCo xO2 cathode after cycle tests in restricted depth of discharge ranges). J. Power Sources *258*, 210–217.
31. Yan, P., Zheng, J., Gu, M., Xiao, J., Zhang, J.G., and Wang, C.M. (2017). Intragranular cracking as a critical barrier for high-voltage usage of layer-structured cathode for lithium-ion batteries. Nat. Commun. *8*, 1–9.
32. Li, T., Yuan, X.-Z., Zhang, L., Song, D., Shi, K., and Bock, C. (2020). Degradation Mechanisms and Mitigation Strategies of Nickel-Rich NMC-Based Lithium-Ion Batteries (Springer Singapore).
33. Hausbrand, R., Cherkashinin, G., Ehrenberg, H., Gröting, M., Albe, K., Hess, C., and Jaegermann, W. (2015). Fundamental degradation mechanisms of layered oxide Li-ion

battery cathode materials: Methodology, insights and novel approaches. Mater. Sci. Eng. B Solid-State Mater. Adv. Technol. *192*, 3–25.

34. Cambaz, M.A., Vinayan, B.P., Geßwein, H., Schiele, A., Sarapulova, A., Diemant, T., Mazilkin, A., Brezesinski, T., Behm, R.J., Ehrenberg, H., et al. (2019). Oxygen Activity in Li-Rich Disordered Rock-Salt Oxide and the Influence of LiNbO3 Surface Modification on the Electrochemical Performance. Chem. Mater. *31*, 4330–4340.
35. Luo, K., Roberts, M.R., Hao, R., Guerrini, N., Pickup, D.M., Liu, Y.S., Edström, K., Guo, J., Chadwick, A. V., Duda, L.C., et al. (2016). Charge-compensation in 3d-transition-metal-oxide intercalation cathodes through the generation of localized electron holes on oxygen. Nat. Chem. *8*, 684–691.
36. Yan, P., Zheng, J., Tang, Z.K., Devaraj, A., Chen, G., Amine, K., Zhang, J.G., Liu, L.M., and Wang, C. (2019). Injection of oxygen vacancies in the bulk lattice of layered cathodes. Nat. Nanotechnol. *14*, 602–608.
37. Wang, L., Wu, B., Mu, D., Liu, X., Peng, Y., Xu, H., Liu, Q., Gai, L., and Wu, F. (2016). Single-crystal LiNi 0.6 Co 0.2 Mn 0.2 O 2 as high performance cathode materials for Li-ion batteries. J. Alloys Compd. *674*, 360–367.
38. Li, J., Li, H., Stone, W., Weber, R., Hy, S., and Dahn, J.R. (2017). Synthesis of Single Crystal LiNi 0.5 Mn 0.3 Co 0.2 O 2 for Lithium Ion Batteries . J. Electrochem. Soc. *164*, A3529–A3537.
39. Mizushima, K., Jones, P.C., Wiseman, P.J., and Goodenough, J.B. (1980). LixCoO2 (0<x<-1): A new cathode material for batteries of high energy density. Mater. Res. Bull. *15*, 783–789.
40. Huggins, R.A. (2010). Energy storage (Springer US).
41. Liu, Q., Su, X., Lei, D., Qin, Y., Wen, J., Guo, F., Wu, Y.A., Rong, Y., Kou, R., Xiao, X., et al. (2018). Approaching the capacity limit of lithium cobalt oxide in lithium ion batteries via lanthanum and aluminium doping. Nat. Energy *3*, 936–943.
42. Wang, X., Gaustad, G., and Babbitt, C.W. (2016). Targeting high value metals in lithium-ion battery recycling via shredding and size-based separation. Waste Manag. *51*, 204–213.
43. Or, T., Gourley, S.W.D., Karthikeyan, K., Yu, A., and Chen, Z. (2020). Recycling of mixed cathode lithium - ion batteries for electric vehicles : Current status and future outlook. Carbon Energy.

44. Bruce, P.G., Scrosati, B., and Tarascon, J.M. (2008). Nanomaterials for rechargeable lithium batteries. Angew. Chemie - Int. Ed. *47*, 2930–2946.
45. Padhi, A.K. (1997). Phospho-olivines as Positive-Electrode Materials for Rechargeable Lithium Batteries. J. Electrochem. Soc. *144*, 1188.
46. Yang, S., Zavalij, P.Y., and Whittingham, M.S. (2001). Hydrothermal Synthesis of Lithium Iron Phosphate Cathodes and Its Electrochemical Performance. Electrochem. commun. *3*, 505–508.
47. Yamada, A., Chung, S.C., and Hinokuma, K. (2001). Optimized LiFePO[sub 4] for Lithium Battery Cathodes. J. Electrochem. Soc. *148*, A224.
48. Lung-Hao Hu, B., Wu, F.Y., Lin, C. Te, Khlobystov, A.N., and Li, L.J. (2013). Graphene-modified LiFePO4 cathode for lithium ion battery beyond theoretical capacity. Nat. Commun. *4*, 1–7.
49. Zeng, X., Li, M., Abd El-Hady, D., Alshitari, W., Al-Bogami, A.S., Lu, J., and Amine, K. (2019). Commercialization of Lithium Battery Technologies for Electric Vehicles. Adv. Energy Mater. *9*, 1900161.
50. International Energy Agency (2019). Global EV Outlook 2019: Scaling-up the transition to electric mobility.
51. Ohzuku, T., and Makimura, Y. (2001). Layered lithium insertion material of LiNi1/2Mn1/2O2 : A possible alternative to LiCoO2 for advanced lithium-ion batteries. Chem. Lett. *2*, 744–745.
52. Ohzuku, T., and Makimura, Y. (2001). Layered lithium insertion material of LiCo1/3Ni1/3Mn1/3O2 for lithium-ion batteries. Chem. Lett., 642–643.
53. Koyama, Y., Yabuuchi, N., Tanaka, I., Adachi, H., and Ohzuku, T. (2004). Solid-State Chemistry and Electrochemistry of LiCo[sub 1/3]Ni[sub 1/3]Mn[sub 1/3]O[sub 2] for Advanced Lithium-Ion Batteries. J. Electrochem. Soc. *151*, A1545.
54. Myung, S.T., Maglia, F., Park, K.J., Yoon, C.S., Lamp, P., Kim, S.J., and Sun, Y.K. (2017). Nickel-Rich Layered Cathode Materials for Automotive Lithium-Ion Batteries: Achievements and Perspectives. ACS Energy Lett. *2*, 196–223.
55. BU-1003: Electric Vehicle (EV) – Battery University https://batteryuniversity.com/learn/article/electric_vehicle_ev.
56. Guilmard, M., Rougier, A., Grüne, M., Croguennec, L., and Delmas, C. (2003). Effects of

aluminum on the structural and electrochemical properties of LiNiO2. J. Power Sources *115*, 305–314.

57. Guilmard, M., Pouillerie, C., Croguennec, L., and Delmas, C. (2003). Structural and electrochemical properties of LiNi0.70Co0.15Al0.15O2. Solid State Ionics *160*, 39–50.
58. Or, T., Gourley, S.W.D., Kaliyappan, K., Yu, A., and Chen, Z. (2020). Recycling of mixed cathode lithium-ion batteries for electric vehicles: Current status and future outlook. Carbon Energy *2*, 6–43.
59. Olivetti, E.A., Ceder, G., Gaustad, G.G., and Fu, X. (2017). Lithium-Ion Battery Supply Chain Considerations: Analysis of Potential Bottlenecks in Critical Metals. Joule *1*, 229–243.
60. Reed, J., and Ceder, G. (2004). Role of electronic structure in the susceptibility of metastable transition-metal oxide structures to transformation. Chem. Rev. *104*, 4513–4533.
61. Clément, R.J., Lun, Z., and Ceder, G. (2020). Cation-disordered rocksalt transition metal oxides and oxyfluorides for high energy lithium-ion cathodes. Energy Environ. Sci. *13*, 345–373.
62. Urban, A., Lee, J., and Ceder, G. (2014). The configurational space of rocksalt-type oxides for high-capacity lithium battery electrodes. Adv. Energy Mater. *4*, 1–9.
63. Urban, A., Abdellahi, A., Dacek, S., Artrith, N., and Ceder, G. (2017). Electronic-Structure Origin of Cation Disorder in Transition-Metal Oxides. Phys. Rev. Lett. *119*, 1–6.
64. Dominko, R., Garrido, C.V.A., Bele, M., Kuezma, M., Arcon, I., and Gaberscek, M. (2011). Electrochemical characteristics of Li2-xVTiO4 rock salt phase in Li-ion batteries. J. Power Sources *196*, 6856–6862.
65. Yabuuchi, N., Takeuchi, M., Komaba, S., Ichikawa, S., Ozaki, T., and Inamasu, T. (2016). Synthesis and electrochemical properties of Li1.3Nb0.3V0.4O2 as a positive electrode material for rechargeable lithium batteries. Chem. Commun. *52*, 2051–2054.
66. Lee, J., Seo, D.H., Balasubramanian, M., Twu, N., Li, X., and Ceder, G. (2015). A new class of high capacity cation-disordered oxides for rechargeable lithium batteries: Li-Ni-Ti-Mo oxides. Energy Environ. Sci. *8*, 3255–3265.
67. Lee, J., Kitchaev, D.A., Kwon, D.H., Lee, C.W., Papp, J.K., Liu, Y.S., Lun, Z., Clément, R.J., Shi, T., McCloskey, B.D., et al. (2018). Reversible Mn2+/Mn4+ double redox in

lithium-excess cathode materials. Nature *556*, 185–190.

68. Seo, D.H., Lee, J., Urban, A., Malik, R., Kang, S., and Ceder, G. (2016). The structural and chemical origin of the oxygen redox activity in layered and cation-disordered Li-excess cathode materials. Nat. Chem. *8*, 692–697.
69. Lee, E., and Persson, K.A. (2014). Structural and Chemical Evolution of the Layered Li-Excess LixMnO3 as a Function of Li Content from First-Principles Calculations. Adv. Energy Mater. *4*, 1–8.
70. Yabuuchi, N., Takeuchi, M., Nakayama, M., Shiiba, H., Ogawa, M., Nakayama, K., Ohta, T., Endo, D., Ozaki, T., Inamasu, T., et al. (2015). High-capacity electrode materials for rechargeable lithium batteries: Li3NbO4-based system with cation-disordered rocksalt structure. Proc. Natl. Acad. Sci. U. S. A. *112*, 7650–7655.
71. Lee, J., Urban, A., Li, X., Su, D., Hautier, G., and Ceder, G. (2014). Unlocking the potential of cation-disordered oxides for rechargeable lithium batteries. Science (80-.). *343*, 519–522.
72. Chong, S., Chen, Y., Yan, W., Guo, S., Tan, Q., Wu, Y., Jiang, T., and Liu, Y. (2016). Suppressing capacity fading and voltage decay of Li-rich layered cathode material by a surface nano-protective layer of CoF2 for lithium-ion batteries. J. Power Sources *332*, 230–239.
73. Pan, H., Zhang, S., Chen, J., Gao, M., Liu, Y., Zhu, T., and Jiang, Y. (2018). Li- and Mn-rich layered oxide cathode materials for lithium-ion batteries: A review from fundamentals to research progress and applications. Mol. Syst. Des. Eng. *3*, 748–803.
74. Zhang, H.Z., Qiao, Q.Q., Li, G.R., Ye, S.H., and Gao, X.P. (2012). Surface nitridation of Li-rich layered Li(Li0.17Ni 0.25Mn0.58)O2 oxide as cathode material for lithium-ion battery. J. Mater. Chem. *22*, 13104–13109.
75. Elam, J.W., Dasgupta, N.P., and Prinz, F.B. (2011). ALD for clean energy conversion, utilization, and storage. MRS Bull. *36*, 899–906.
76. Meng, X., Yang, X.Q., and Sun, X. (2012). Emerging applications of atomic layer deposition for lithium-ion battery studies. Adv. Mater. *24*, 3589–3615.
77. Hassan, F.M., Batmaz, R., Li, J., Wang, X., Xiao, X., Yu, A., and Chen, Z. (2015). Evidence of covalent synergy in silicon-sulfur-graphene yielding highly efficient and long-life lithium-ion batteries. Nat. Commun. *6*, 1–11.

78. Lin, W., Wang, J., Zhou, R., Wu, B., and Zhao, J. (2017). Improving the electrochemical performance of LiNi0.5Mn1.5O4 cathode materials by surface coating with cyclized polyacrylonitrile for lithium-ion batteries. Int. J. Electrochem. Sci. *12*, 12047–12059.
79. Linden, D., Reddy Editor, T.B., York, N., San, C., Lisbon, F., Madrid, L., City, M., New, M., San, D., and Seoul, J. (2002). HANDBOOK OF BATTERIES.
80. Lee, M.H., Kang, Y.J., Myung, S.T., and Sun, Y.K. (2004). Synthetic optimization of Li[Ni1/3Co1/3Mn 1/3]O2 via co-precipitation. Electrochim. Acta *50*, 939–948.
81. Lee, K.S., Myung, S.T., Moon, J.S., and Sun, Y.K. (2008). Particle size effect of Li[Ni0.5Mn0.5]O2 prepared by co-precipitation. Electrochim. Acta *53*, 6033–6037.
82. Wang, D., Belharouak, I., Koenig, G.M., Zhou, G., and Amine, K. (2011). Growth mechanism of Ni0.3Mn0.7CO3 precursor for high capacity Li-ion battery cathodes. J. Mater. Chem. *21*, 9290–9295.
83. Li, H., Li, J., Ma, X., and Dahn, J.R. (2018). Synthesis of Single Crystal LiNi 0.6 Mn 0.2 Co 0.2 O 2 with Enhanced Electrochemical Performance for Lithium Ion Batteries . J. Electrochem. Soc. *165*, A1038–A1045.
84. Emel'chenko, G.A., Masalov, V.M., and Tatarchenko, V.A. (1992). Controlled Flux Growth of Complex Oxide Single Crystals. In Growth of Crystals (Springer US), pp. 121–134.
85. Kan, W.H., Deng, B., Xu, Y., Shukla, A.K., Bo, T., Zhang, S., Liu, J., Pianetta, P., Wang, B.T., Liu, Y., et al. (2018). Understanding the Effect of Local Short-Range Ordering on Lithium Diffusion in Li1.3Nb0.3Mn0.4O2 Single-Crystal Cathode. Chem *4*, 2108–2123.
86. Shi, S.J., Tu, J.P., Tang, Y.Y., Liu, X.Y., Zhao, X.Y., Wang, X.L., and Gu, C.D. (2013). Morphology and electrochemical performance of Li[Li0.2Mn 0.54Ni0.13Co0.13]O2 cathode materials treated in molten salts. J. Power Sources *241*, 186–195.
87. Boltersdorf, J., King, N., and Maggard, P.A. (2015). Flux-mediated crystal growth of metal oxides: Synthetic tunability of particle morphologies, sizes, and surface features for photocatalysis research. CrystEngComm *17*, 2225–2241.
88. Zong, Y., Guo, Z., Xu, T., Liu, C., Li, Y., and Yang, G. (2020). Flux preparation of LiNi0.6Co0.2Mn0.2 micron-sized crystals as cathode materials for highly reversible lithium storage. Int. J. Energy Res., 1–10.
89. Kremer, L.S., Hoffmann, A., Danner, T., Hein, S., Prifling, B., Westhoff, D., Dreer, C.,

Latz, A., Schmidt, V., and Wohlfahrt-Mehrens, M. (2020). Manufacturing Process for Improved Ultra-Thick Cathodes in High-Energy Lithium-Ion Batteries. Energy Technol. *8*, 1–14.

90. Marks, T., Trussler, S., Smith, A.J., Xiong, D., and Dahn, J.R. (2011). A Guide to Li-Ion Coin-Cell Electrode Making for Academic Researchers. J. Electrochem. Soc. *158*, A51.
91. Park, S.H., King, P.J., Tian, R., Boland, C.S., Coelho, J., Zhang, C. (John), McBean, P., McEvoy, N., Kremer, M.P., Daly, D., et al. (2019). High areal capacity battery electrodes enabled by segregated nanotube networks. Nat. Energy *4*.
92. Karthikeyan, K., Kim, S.H., Kim, K.J., Lee, S.N., and Lee, Y.S. (2013). Low cost, eco-friendly layered Li1.2(Mn0.32Ni 0.32Fe0.16)O2nanoparticlesfor hybrid supercapacitor applications. Electrochim. Acta *109*, 595–601.
93. Murray, V., Hall, D.S., and Dahn, J.R. (2019). A Guide to Full Coin Cell Making for Academic Researchers. J. Electrochem. Soc. *166*, A329–A333.
94. Lux, S.F., Chevalier, J., Lucas, I.T., and Kostecki, R. (2013). HF formation in LiPF6-based organic carbonate electrolytes. ECS Electrochem. Lett. *2*, 121–123.
95. Chen, Y., Zhang, Y., Chen, B., Wang, Z., and Lu, C. (2014). An approach to application for LiNi0.6Co0.2Mn 0.2O2 cathode material at high cutoff voltage by TiO 2 coating. J. Power Sources *256*, 20–27.
96. Mohanty, D., Dahlberg, K., King, D.M., David, L.A., Sefat, A.S., Wood, D.L., Daniel, C., Dhar, S., Mahajan, V., Lee, M., et al. (2016). Modification of Ni-Rich FCG NMC and NCA Cathodes by Atomic Layer Deposition: Preventing Surface Phase Transitions for High-Voltage Lithium-Ion Batteries. Sci. Rep. *6*, 1–16.
97. Arumugam, R.S., Ma, L., Li, J., Xia, X., Paulsen, J.M., and Dahn, J.R. (2016). Special Synergy between Electrolyte Additives and Positive Electrode Surface Coating to Enhance the Performance of Li[Ni 0.6 Mn 0.2 Co 0.2]O 2 /Graphite Cells . J. Electrochem. Soc. *163*, A2531–A2538.
98. Hall, D.S., Gauthier, R., Eldesoky, A., Murray, V.S., and Dahn, J.R. (2019). New Chemical Insights into the Beneficial Role of Al 2 O 3 Cathode Coatings in Lithium-ion Cells. ACS Appl. Mater. Interfaces *11*, 14095–14100.
99. Lee, S., Kim, J., and Shin, D. (2007). Modification of network structure induced by glass former composition and its correlation to the conductivity in lithium borophosphate glass

for solid state electrolyte. Solid State Ionics *178*, 375–379.

100. Cho, K.I., Lee, S.H., Cho, K.H., Shin, D.W., and Sun, Y.K. (2006). Li2O-B2O3-P2O5 solid electrolyte for thin film batteries. J. Power Sources *163*, 223–228.
101. Muñoz, F., Montagne, L., Pascual, L., and Durán, A. (2009). Composition and structure dependence of the properties of lithium borophosphate glasses showing boron anomaly. J. Non. Cryst. Solids *355*, 2571–2577.
102. Yan, P., Zheng, J., Liu, J., Wang, B., Cheng, X., Zhang, Y., Sun, X., Wang, C., and Zhang, J.G. (2018). Tailoring grain boundary structures and chemistry of Ni-rich layered cathodes for enhanced cycle stability of lithium-ion batteries. Nat. Energy *3*, 600–605.
103. Du, C., Yang, M., Liu, J., Sun, S., Tang, Z., Qu, D., and Zhang, X. (2015). Surface modification of a LiNi0.5Mn1.5O4 cathode with lithium boron oxide glass for lithium-ion batteries. RSC Adv. *5*, 57293–57299.
104. Goldstein, J., Newbury, D.E., Joy, D.C., Lyman, C.E., Echlin, P., Lifshin, E., Sawyer, L., Michael, J.R. (2003). Scanning Electron Microscopy and X-ray Microanalysis - | Joseph Goldstein | Springer (Springer US).
105. Richard, M.N. (1999). Accelerating Rate Calorimetry Study on the Thermal Stability of Lithium Intercalated Graphite in Electrolyte. II. Modeling the Results and Predicting Differential Scanning Calorimeter Curves. J. Electrochem. Soc. *146*, 2078.
106. Saadatkhah, N., Carillo Garcia, A., Ackermann, S., Leclerc, P., Latifi, M., Samih, S., Patience, G.S., and Chaouki, J. (2020). Experimental methods in chemical engineering: Thermogravimetric analysis—TGA. Can. J. Chem. Eng. *98*, 34–43.
107. Ma, S., Jiang, M., Tao, P., Song, C., Wu, J., Wang, J., Deng, T., and Shang, W. (2018). Temperature effect and thermal impact in lithium-ion batteries: A review. Prog. Nat. Sci. Mater. Int. *28*, 653–666.
108. Cormier, M.M.E., Zhang, N., Liu, A., Li, H., Inglis, J., and Dahn, J.R. (2019). Impact of Dopants (Al, Mg, Mn, Co) on the Reactivity of Li x NiO 2 with the Electrolyte of Li-Ion Batteries . J. Electrochem. Soc. *166*, A2826–A2833.
109. Basics of Electrochemical Impedance Spectroscopy.
110. Studying Impedance to Analyze the Li-Ion Battery with an App | COMSOL Blog https://www.comsol.com/blogs/studying-impedance-to-analyze-the-li-ion-battery-with-an-app/.

111. Smith, A.J., and Dahn, J.R. (2012). Delta Differential Capacity Analysis. J. Electrochem. Soc. *159*, A290–A293.
112. Dahn, H.M., Smith, A.J., Burns, J.C., Stevens, D.A., and Dahn, J.R. (2012). User-Friendly Differential Voltage Analysis Freeware for the Analysis of Degradation Mechanisms in Li-Ion Batteries. J. Electrochem. Soc. *159*, A1405–A1409.
113. Zheng, L., Zhu, J., Lu, D.D.C., Wang, G., and He, T. (2018). Incremental capacity analysis and differential voltage analysis based state of charge and capacity estimation for lithium-ion batteries. Energy *150*, 759–769.
114. Han, X., Feng, X., Ouyang, M., Lu, L., Li, J., Zheng, Y., and Li, Z. (2019). A Comparative Study of Charging Voltage Curve Analysis and State of Health Estimation of Lithium-ion Batteries in Electric Vehicle. Automot. Innov. *2*, 263–275.
115. Wang, R., Li, X., Liu, L., Lee, J., Seo, D.H., Bo, S.H., Urban, A., and Ceder, G. (2015). A disordered rock-salt Li-excess cathode material with high capacity and substantial oxygen redox activity: Li1.25Nb0.25Mn0.5O2. Electrochem. commun. *60*, 70–73.
116. Kim, J., Lee, H., Cha, H., Yoon, M., Park, M., and Cho, J. (2018). Prospect and Reality of Ni-Rich Cathode for Commercialization. Adv. Energy Mater. *8*, 1–25.
117. Zhang, T., Li, J.T., Liu, J., Deng, Y.P., Wu, Z.G., Yin, Z.W., Guo, D., Huang, L., and Sun, S.G. (2016). Suppressing the voltage-fading of layered lithium-rich cathode materials via an aqueous binder for Li-ion batteries. Chem. Commun. *52*, 4683–4686.
118. Li, J., Daniel, C., An, S.J., and Wood, D. (2016). Evaluation residual moisture in lithium-ion battery electrodes and its effect on electrode performance. MRS Adv. *1*, 1029–1035.
119. Huttner, F., Haselrieder, W., and Kwade, A. (2020). The Influence of Different Post-Drying Procedures on Remaining Water Content and Physical and Electrochemical Properties of Lithium-Ion Batteries. Energy Technol. *8*, 1–11.
120. TDK-Lambda Americas Blog: Constant Voltage, Constant Current Battery Charging http://power-topics.blogspot.com/2016/05/constant-voltage-constant-current.html.
121. Xu, G.L., Liu, Q., Lau, K.K.S., Liu, Y., Liu, X., Gao, H., Zhou, X., Zhuang, M., Ren, Y., Li, J., et al. (2019). Building ultraconformal protective layers on both secondary and primary particles of layered lithium transition metal oxide cathodes. Nat. Energy *4*, 484–494.